AGU PUBLICATIONS

Water Resources Research

RESEARCH ARTICLE
10.1002/2016WR018935

This article is a companion to *Bao et al.* [2017], doi:10.1002/2016WR018934.

Special Section:
Concentration-discharge Relations in the Critical Zone

Understanding watershed hydrogeochemistry: 2. Synchronized hydrological and geochemical processes drive stream chemostatic behavior

Li Li[1], Chen Bao[2], Pamela L. Sullivan[3,4], Susan Brantley[3], Yuning Shi[5], and Christopher Duffy[1]

[1]Department of Civil and Environmental Engineering, Pennsylvania State University, University Park, Pennsylvania, USA, [2]John and Willie Leone Department of Energy and Mineral Engineering, Pennsylvania State University, University Park, Pennsylvania, USA, [3]Earth and Environmental Systems Institute, and Department of Geosciences, Pennsylvania State University, University Park, Pennsylvania, USA, [4]Now at Department of Geography, University of Kansas, Lawrence, Kansas, USA, [5]Department of Ecosystem Science and Management, Pennsylvania State University, University Park, Pennsylvania, USA

Abstract Why do solute concentrations in streams remain largely constant while discharge varies by orders of magnitude? We used a new hydrological land surface and reactive transport code, RT-Flux-PIHM, to understand this long-standing puzzle. We focus on the nonreactive chloride (Cl) and reactive magnesium (Mg) in the Susquehanna Shale Hills Critical Zone Observatory (SSHCZO). Simulation results show that stream discharge comes from surface runoff (Q_S), soil lateral flow (Q_L), and deeper groundwater (Q_G), with Q_L contributing >70%. In the summer, when high evapotranspiration dries up and disconnects most of the watershed from the stream, Cl is trapped along planar hillslopes. Successive rainfalls connect the watershed and mobilize trapped Cl, which counteracts dilution effects brought about by high water storage (V_w) and maintains chemostasis. Similarly, the synchronous response of clay dissolution rates (Mg source) to hydrological conditions, maintained largely by a relatively constant ratio between "wetted" mineral surface area A_w and V_w, controls Mg chemostatic behavior. Sensitivity analysis indicates that cation exchange plays a secondary role in determining chemostasis compared to clay dissolution, although it does store an order-of-magnitude more Mg on exchange sites than soil water. Model simulations indicate that dilution (concentration decrease with increasing discharge) occurs only when mass influxes from soil lateral flow are negligible (e.g., via having low clay surface area) so that stream discharge is dominated by relatively constant mass fluxes from deep groundwater that are unresponsive to surface hydrological conditions.

Key Points:
- A new watershed hydrogeochemistry code, RT-Flux-PIHM, allows deeper understanding of chemostatic behavior in stream discharge
- Chemostasis is driven by synchronized geochemical (clay dissolution and Cl mobilization) and hydrological processes
- Dilution occurs when stream discharge is dominated by relatively constant and hydrologically unresponsive deep groundwater influxes

Correspondence to:
L. Li,
lili@engr.psu.edu

Citation:
Li, L., C. Bao, P. L. Sullivan, S. Brantley, Y. Shi, and C. Duffy (2017), Understanding watershed hydrogeochemistry: 2. Synchronized hydrological and geochemical processes drive stream chemostatic behavior, *Water Resour. Res.*, *53*, 2346–2367, doi:10.1002/2016WR018935.

Received 14 MAR 2016
Accepted 8 FEB 2017
Accepted article online 15 FEB 2017
Published online 23 MAR 2017

1. Introduction

Solute concentration (C) and discharge (Q) at stream mouths integrate water and reaction processes dictated by land cover, topography and subsurface structure, encoding important signatures of hydrology and geochemical coupling at the watershed scale (Figure 1). Concentration-discharge (CQ) relationships are important for understanding watershed response to hydrological conditions [*Anderson et al.*, 1997; *Godsey et al.*, 2009], for estimating export of solute fluxes out of watersheds [*Basu et al.*, 2010b; *Ferguson*, 1986; *Stenback et al.*, 2011], and for quantifying chemical weathering at the watershed scale [*Gaillardet et al.*, 1999; *Navarre-Sitchler and Brantley*, 2007; *Raymond and Cole*, 2003; *White and Blum*, 1995].

The CQ relationships of conservative tracers such as chloride (Cl) reflect water flow and nonreactive solute transport; those of geogenic species (e.g., Mg, Na, originated from mineral dissolution) offer signals of chemical weathering; those of biorelevant species, including dissolved organic carbon (DOC), nutrients (N, P), and cations (e.g., Fe, Al) that form complexes with DOC, provide insights into hydrological and biogeochemical process coupling [*Basu et al.*, 2010b; *Boyer et al.*, 1997; *Grimm et al.*, 2003; *Sebestyen et al.*, 2014, 2008]. The CQ relationships usually follow power laws in the form of $C=aQ^b$, where a and b are constants. For C and Q in a logarithmic scale, reported b values (i.e., slopes of log C versus log Q relationship) vary from +0.4 to −0.7 but mostly cluster between 0 and ±0.20 [*Godsey et al.*, 2009; *Herndon et al.*, 2015]. The CQ relationships are considered *chemostatic* when the b values are within ±0.20, indicating relatively small variations in concentrations compared to large variations in discharge. In contrast, if concentrations decrease

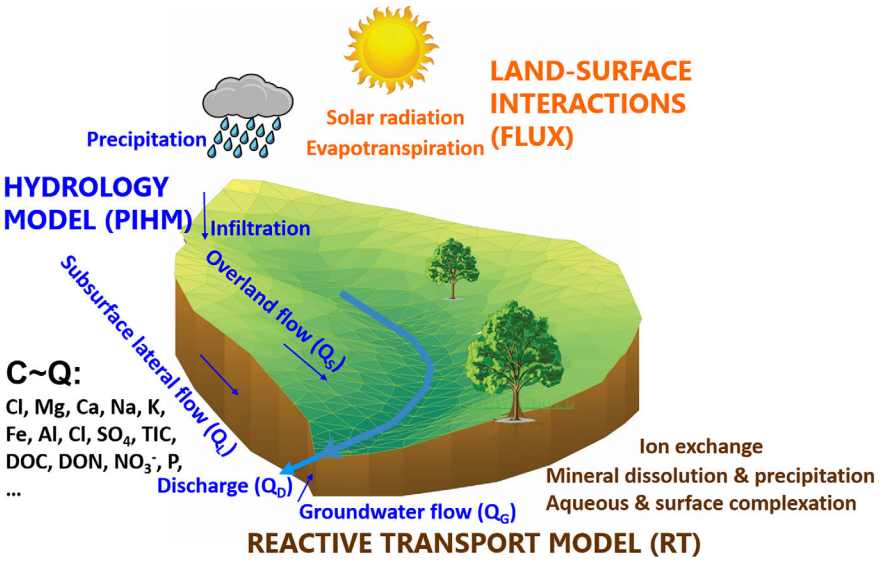

Figure 1. A schematic representation of processes in different modules (different colors) of RT-Flux-PIHM. The model allows systematic understanding of coupled processes at the grid and watershed scales. Note that three types of flow contribute to the stream discharge Q_D: overland flow (surface runoff, Q_S), subsurface lateral flow in soil (Q_L), and deep groundwater flow (Q_G).

significantly with increasing discharge with b values more negative than −0.20, the CQ behavior is defined as *dilution*. While one expects variable CQ behaviors under different watershed conditions, this has been shown not necessarily the case. The CQ behavior of nonreactive tracers and geogenic solutes have been observed to be largely chemostatic under a wide range of climate, geology, and hydrology conditions [*Anderson et al*., 1997; *Clow and Mast*, 2010; *Godsey et al*., 2009; *Johnson et al*., 1969; *Peters et al*., 1998; *Stallard and Murphy*, 2014]. The mechanisms of this commonly observed chemostatic behavior, however, are poorly understood and present a long-standing puzzle in watershed hydrogeochemistry [*Kirchner*, 2003].

Efforts to explain the CQ puzzle date back to more than half a century ago [*Johnson et al*., 1969]. The Cl chemostasis has been interpreted by low dimension homogeneous bucket models [*Duffy and Cusumano*, 1998; *Gelhar and Wilson*, 1974] and by catchment-scale dispersion processes [*Kirchner et al*., 2000, 2001] as caused by long solute residence time in soil relative to the short hydrological response time. It has also been explained as due to the mixing of different source waters, including old shallow soil water stored in the watershed, new rainfall water, and deep groundwater [*Bishop et al*., 2004; *Chanat et al*., 2002; *Evans and Davies*, 1998; *Hooper et al*., 1990; *Johnson et al*., 1969; *Stallard and Murphy*, 2014]. The chemostasis of geogenic cations from chemical weathering has been attributed to several mechanisms. *Godsey et al*. [2009] used a permeability-porosity-aperture model to argue that increases in mineral surface area during high discharge conditions dissolve more solutes, therefore counteracting dilution effects and maintaining chemostasis. *Maher* [2011] suggested that sufficiently long residence times allow mineral dissolution to reach equilibrium and lead to chemostatic behavior. *Herndon et al*. [2015] attributed chemostasis to homogeneous distributions of soil minerals and quick release of cations from exchange sites during rainfall events. Cation exchange has been considered as important in setting the limits in stream concentrations and in organic-mineral interactions [*Clow and Mast*, 2010; *Hoagland, et al*., 2017]. The CQ relationships from steep mountain catchments have been observed to be more chemostatic relative to those from shallow foreland floodplain, indicating important links between geomorphic regimes, flow characteristics, and CQ relationships [*Jin et al*., 2010; *Torres et al*., 2015].

The above mentioned studies provide hypotheses on mechanisms of chemostatic behavior and have not yet reconciled different CQ observations. Most existing studies focus on particular geochemical or hydrological aspects without integrating interdependent processes and watershed spatial complexity. A spatially explicit and process-based approach can provide a platform to probe process interdependence and to differentiate the relative dominance of individual processes. Here we use RT-Flux-PIHM, a recently developed code that integrates hydrological, land surface, and multicomponent reactive transport processes at the watershed scale [*Bao et al*., 2017], to understand hydrogeochemical coupling in the Susquehanna Shale Hills

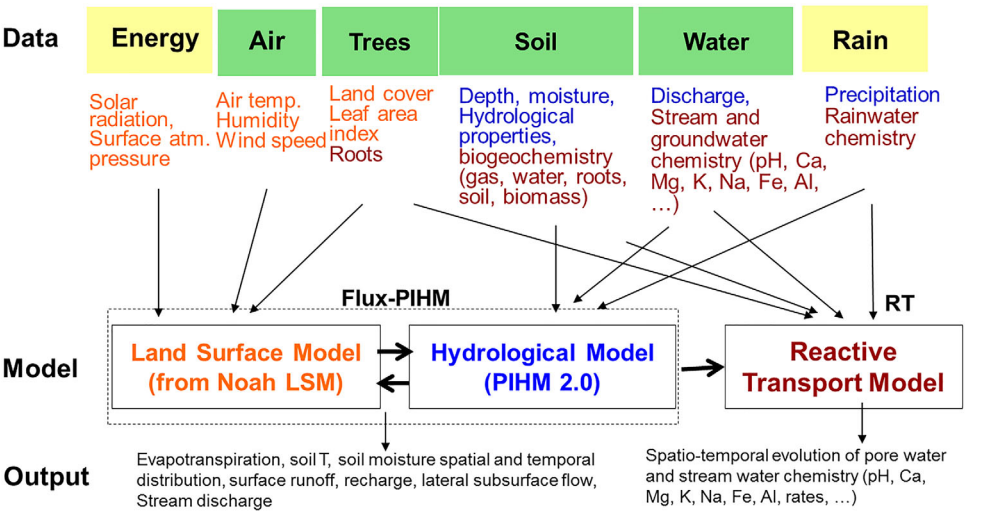

Figure 2. Data types and data-model integration structure. The yellow boxes indicate data from national databases; the green boxes indicate measurements at the SSHCZO site. The font color indicates connections between data and modules: orange-colored data for the orange-colored LSM; blue-colored and brown-colored data for PIHM and RT, respectively.

Critical Zone Observatory (SSHCZO) [*Brantley et al.*, 2006; *Duffy et al.*, 2009]. We focus on the chemostasis of the nonreactive Cl and reactive Mg. Chloride originates from precipitation while Mg dissolves out of clay weathering and participates in ion exchange reactions. We found that chemostatic behavior is largely driven by the synchronized response of soil water content (and subsurface lateral flow) and geochemical reactions (weathering for Mg and solute mobilization for Cl) to surface hydrological conditions.

2. The Model, Study Site, and Data-Model Integration

2.1. The Watershed Hydrogeochemical Code RT-Flux-PIHM

As discussed in the companion model development paper [*Bao et al.*, 2017] and illustrated in Figure 1, RT-Flux-PIHM integrates several processes. The PIHM and Flux modules solve for the spatiotemporal evolution of temperature and water, including water saturation and fluxes (e.g., infiltration, recharge, lateral flow into the stream) [*Qu and Duffy*, 2007; *Shi et al.*, 2013]. The lateral flow in the shallow soil water (saturated zone) has been observed to be the largest contributor to stream discharge in SSHCZO. The RT module takes water outputs from Flux-PIHM and calculates the spatial and temporal distribution of aqueous and solid concentrations by explicitly including reaction kinetics and thermodynamics for mineral dissolution and precipitation, aqueous complexation, and cation exchange. Mineral dissolution and precipitation are described through kinetic rate laws and equilibrium while aqueous complexation and ion exchange are treated strictly as at equilibrium. Note that Flux-PIHM does not explicitly simulate deep regional ground water measured tens of meters below the ridges. We consider the groundwater influx from the deep subsurface by adding a constant water and mass influx based on field measurements, as will be discussed later. The groundwater is referred to as "deep groundwater" for the rest of the manuscript (Q_G in Figure 1).

2.2. Data-Model Integration

We apply RT-Flux-PIHM to SSHCZO, a V-shaped, first order watershed in central Pennsylvania (0.08 km^2) [*Lin*, 2006]. The mean annual temperature is 10°C with a mean annual precipitation of 1070 mm [*Jin et al.*, 2011a]. Extensive measurements have been conducted to characterize the topography, hydrological properties and mineral composition [*Brantley et al.*, 2013a; *Jin et al.*, 2011b, 2010; *Lin*, 2006; *Ma et al.*, 2010]. Watershed characteristics include topography (e.g., soil depth, surface elevation), soil properties (e.g., soil type, soil hydraulic conductivity, porosity, macro pore conductivity, van Genuchten parameters), and vegetation properties (e.g., land cover, rooting depth) [*Shi et al.*, 2013] (Figure 2). The USGS National Elevation Dataset (NED) and National Land Cover Database (NLCD) provide topography and land cover map with a priori parameters. These data were used initially and were refined later whenever specific measurements were available. Watershed initial and boundary conditions include subsurface characteristics (e.g., soil

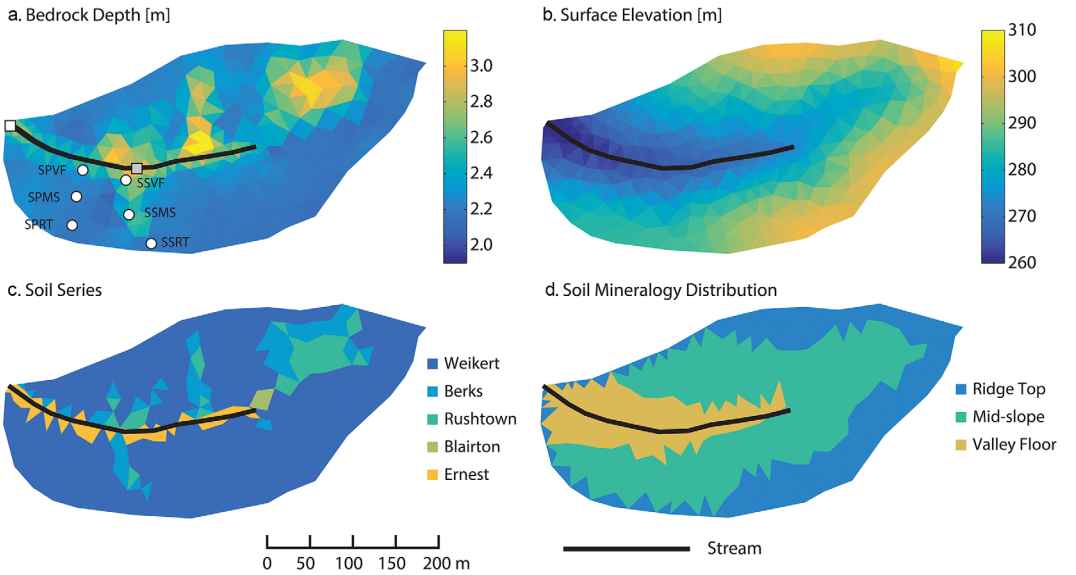

Figure 3. Topographic and soil property map based on field surveys. (a) Depth to measured nonaugerable, impermeable bedrock (m) [*Lin*, 2006] with symbols representing sampling points; (b) surface elevation (m); (c) soil series; (d) zones of geochemical initial conditions assigned based on field measurements [*Jin et al*., 2010]. Stream discharge measured at the weir (white square) and the groundwater table depth measured at the groundwater well in the stream riparian zone (grey square) were used to calibrate Flux-PIHM [*Shi et al*., 2013]. Water chemistry was measured in (1) lysimeter nests at the south planar sites—valley floor (SPVF), midslope (SPMS) and ridgetop (SPRT), and at south swale sites—valley floor (SSVF), midslope (SSMS) and ridgetop (SSRT); (2) the weir at the stream mouth. Measured compositions of stream and soil water were used to calibrate RT. The swales are hillslope zones of convergent flow whereas the planar hillslopes are zones of nonconvergent flow.

depth), initial water distribution, water table, snow cover, canopy storage and watershed boundary fluxes. Ecohydrological processes were constrained using time series forcing data either measured at the site or from National Land Data Assimilation Systems Phase 2 (NLDAS-2). These include precipitation, air temperature, wind speed, solar radiation, leaf area index, discharge, and surface heat fluxes.

Measured depths of hand-augerable soil from the ground surface vary from less than 0.25 m at ridge top to 1.87 m in valley floor [*Lin*, 2006]. At the bottom of this soil, the depth of permeable fractured saprock has been quantified at a few boreholes and is known to extend to several meters depth [*Brantley et al*., 2013a]. We therefore follow the convention of previous Flux-PIHM simulations [*Kumar et al*., 2009; *Qu and Duffy*, 2007] and stipulate that the thickness of the deep saprock layer is 1.5 m and that beneath that layer, the "bedrock" is impermeable across SSHCZO. The shallow subsurface thickness, i.e., the summation of the soil layer and fractured saprock above the bedrock, therefore varies from 1.75 to 3.37 m. The spatial distribution of soil types and soil matrix properties (including porosity and permeability) are from field survey and have been discussed in previous work [*Lin*, 2006; *Shi et al*., 2013]. Measured hydraulic conductivities are used as a priori values [*Kuntz et al*., 2011] and tuned to reproduce discharge and groundwater level data [*Shi et al*., 2013]. Hydrological and geochemical processes have been monitored at high temporal resolution at selected locations. These include stream discharge, groundwater table depth, soil moisture, air temperature, stream chemistry and soil water chemistry in 12 lysimeter nests, 6 of which are shown in Figure 3 [*Duffy et al*., 2014]. Geochemical conditions are constrained based on measured soil and water chemistry (e.g., water composition, mineral composition, surface area, and ion exchange capacity) and soil gases [*Hasenmueller et al*., 2015; *Jin et al*., 2014]. Soil composition was assumed to be uniform at different depths. Soil chemistry was distributed based on the mineralogical map (Figure 3d) and soil composition (Table 2).

2.3. Hydrological Processes

From 1 April to 31 December 2009, the total precipitation was 0.9 m. As shown in Figure 4a, SSHCZO is hydrologically responsive with stream discharge closely following intensive precipitation events. Total ET increases from spring to summer and then decreases in winter. Although the precipitation is relatively invariant over the year, water storage decreases in the summer due to high ET, which is consistent with observed water level drop in monitoring wells [*Shi et al*., 2013]. The model shows that 39.7% of the

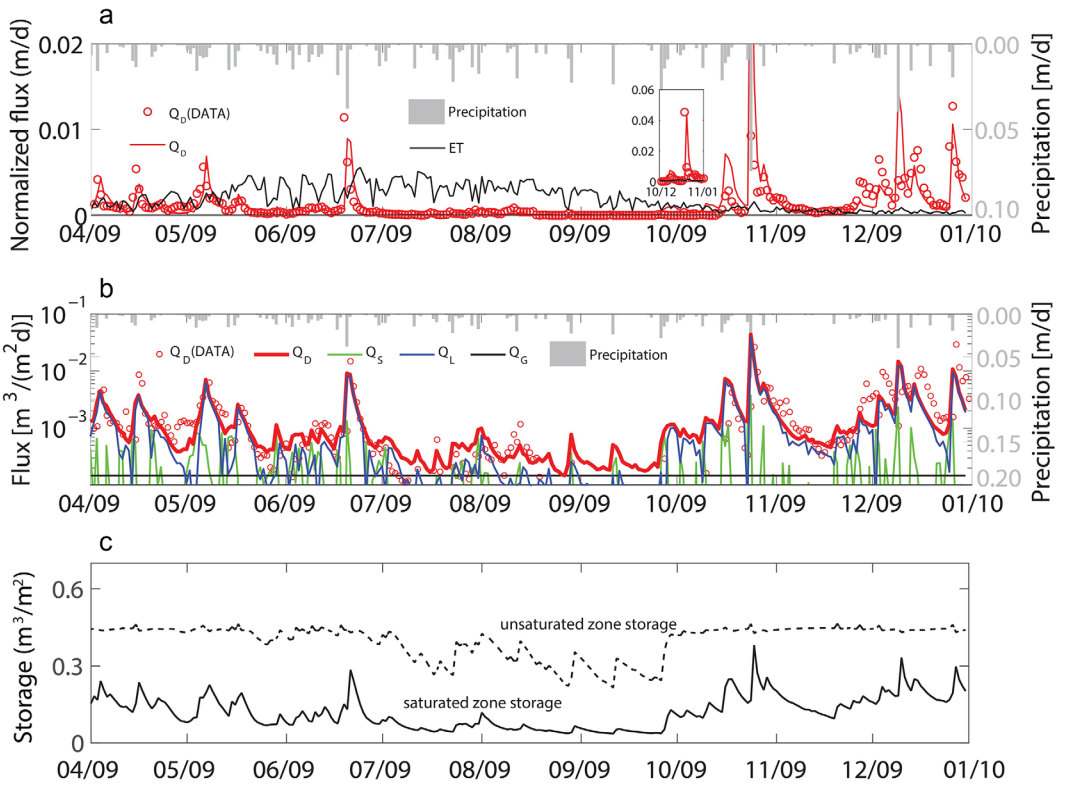

Figure 4. (a) Temporal evolution of measured daily precipitation (m/d), discharge Q_D (m/d), and total ET (m/d), all normalized by land surface area. (b) Contributions to stream discharge (Q_D) from different flows: Q_S: surface runoff (overland flow); Q_L: lateral subsurface flow; Q_G: groundwater influx. (c) Temporal evolution of water storage in the saturated and unsaturated zones (m^3/m^2 land surface) [*Shi et al.*, 2013]. Daily water storage varies seasonally: water storage is higher because of lower ET in spring and winter and is lower because of higher ET in the summer. The model output shows that water storage in the saturated zone is more responsive to rainfall events, indicating that rainfall events primarily raise the shallow water table and increase the thickness of the saturated zone.

precipitation contributes to stream discharge and 58.8% to total ET with the remaining 1.5% as water storage. Watershed-averaged variables were calculated by summing up grid-scale daily modeling output and averaging by the watershed land surface area.

Field observations indicate strong evidence of deep groundwater flow into the stream with chemical compositions different from soil water [*Jin et al.*, 2011a, 2014; *Thomas et al.*, 2013]. The value of the groundwater influx (Q_G) however is not available and was therefore tuned to 1.04×10^{-3} $m^3/m^2/d$ to reproduce stream chemistry, as will be discussed later. This water flux is 6.7% of the calculated 0.015 $m^3/m^2/d$ of average stream discharge in 2009. As shown in Figure 4b, the contribution of different flows varies significantly depending on hydrological conditions. During rainfall events, surface runoff (Q_S) dominates as short-lived pulses in early stages and is followed by subsurface lateral flow (Q_L) with longer time duration. In the summer, when water is lost more through ET, the stream discharge is dominated by Q_G providing base flow. During most of the year, however, Q_L contributes more than 70% of the discharge. This is consistent with tracer and groundwater table data indicating that "The stream receives contributions mainly from groundwater during warmer months characterized by low discharge and by soil waters during high discharge seasons" [*Jin et al.*, 2011a,].

2.4. Chloride Processes

Chloride, a major anion in rainwater, is insignificant in the SSHCZO bedrock and regolith and is therefore controlled by atmospheric or groundwater inputs. Although recent evidence suggests that Cl is not fully conservative [*Bastviken et al.*, 2007], net release/retention has been found to be negligible for most watersheds [*Svensson et al.*, 2012, 2007]. The average chloride concentration ([Cl]) in rainwater in 2009 was 3.05 ($\pm$4.20) μmol/L, as measured at the Leading Ridge as part of the National Atmospheric Deposition Program

[*Lamb and Bowersox*, 2000]. The data from Clean Air Status and Trends Network (CASTNET) (http://epa.gov/castnet/javaweb/index.html) suggest Cl input from dry deposition is about 5 mol in 2009 and accounts for less than 2% of total Cl input from rainwater (~300 mol in 2009). The mass influx from Q_G was calculated as the product of the average groundwater [Cl] (63.62 ± 24.82 μmol/L) [*Brantley et al*., 2013c] and the tuned influx rate into the stream. With the already tuned parameters for hydrological processes in Flux-PIHM [*Shi et al*., 2013], the influx of chloride from deep groundwater is the only tuning parameter used for reproducing Cl data.

The tree canopy intercepts about 40% of rainwater (annual average) [*Shi et al*., 2013]. Some of the incoming salt becomes salt residues on foliage during evaporation, which eventually reaches the ground with litter fall and throughfall. In effect, although not all rainwater passes through the canopy, all solute mass eventually reaches the ground. The throughfall is expected to have higher [Cl] compared to the rainwater [*Svensson et al*., 2012]. Flux-PIHM calculates the water fluxes but not the throughfall composition such that it does not compute the higher solute concentrations in the throughfall. To compensate for this missing process, we calculate the concentrations of all solutes in throughfall by multiplying their rainwater concentration with the annual average volume ratio of precipitation and ET (1.6). The ratio could vary over time and space; for simplicity here we assume a constant value. A diffusion coefficient of 1.0×10^{-9} m^2/s and a dispersivity of 0.1 m were used, both of which are within the reported range at the relevant spatial scale [*Cussler*, 2009; *Gelhar et al*., 1992].

2.5. Reactive Transport of Magnesium

Magnesium comes from three sources: atmospheric deposition, clay dissolution, and groundwater influx [*Jin et al*., 2014]. The [Mg] in rainwater is 1.4 (±1.2) μmol/L on average [*Lamb and Bowersox*, 2000], leading to a total of ~112 mol in 2009. The Mg deposition from dust is about 4.8 mol in 2009 (http://epa.gov/castnet/javaweb/index.html). The overall Mg contribution (~117 mol/yr) from atmospheric deposition is relatively small compared to the annual Mg outflow of about 4700 mol/yr [*Brantley et al*., 2013a] (calculated by multiplying discharge with concentration at the stream mouth). It has been hypothesized that most carbonate is depleted in the upper layers of the watershed [*Brantley et al*., 2013a, 2013b,2013c, 2013d] and that the dissolution of Mg-containing carbonate in the deep groundwater produces Mg-rich groundwater (238.8 ± 109.8 μmol/L) [*Jin et al*., 2011a]. *Jin et al*. [2014] estimate the annual contribution from deep groundwater to be ~1000 mol/yr by comparing [Mg] in stream water and soil water. Therefore, a constant groundwater influx is added as a Mg source to stream water using the same tuned constant groundwater influx rate as used for Cl dynamics. This groundwater influx accounts for about 20% of the total Mg outflow from the stream because of the much higher [Mg] in deep groundwater.

The shallow soil and regolith contains quartz, illite, "chlorite" and kaolinite [*Jin et al*., 2011b,]. We use the term "chlorite" to indicate a mineral showing the same peaks as chlorite in X-ray diffraction traces (XRD); however, it could contain chlorite, vermiculite, hydroxy-interlayered vermiculite, and/or mixtures of these phases [*Jin et al*., 2010; *Moore and Reynolds*, 1989]. "Chlorite" (hereafter, written as chlorite) and illite dissolve and are the major source of Mg. Clay dissolution rates were calculated based on the Transition State Theory (TST) [*Helgeson et al*., 1984; *Lasaga*, 1984]:

$$R_k = A_{w,k} k_k \left(1 - \frac{IAP}{K_{eq}}\right) \tag{1}$$

Here R_k is the dissolution/precipitation rate of mineral k (mol/(m^3 s)); $A_{w,k}$ is the "wetted" dissolving surface area of mineral k per volume of porous media (m^2/m^3); k_k is intrinsic rate constant [mol/(m^2 s)]; IAP is ion activity product; and K_{eq} is reaction equilibrium constant. The "wetted" mineral surface area depends on soil moisture through a power law [*Clow and Mast*, 2010]:

$$A_{w,k} = A_k^0 S_w^n \tag{2}$$

Here A_k^0 is total mineral surface area per volume of porous media under fully saturated conditions. An n value of 2/3 was used to indicate the surface area to volume ratio of mineral grains [*Mayer et al*., 2002].

While magnesium ultimately derives from mineral dissolution, cation exchange is believed to buffer soil water concentrations of ions [*Clow and Mast*, 2010; *Godsey et al*., 2009; *Herndon et al*., 2015; *Jin et al*., 2011a]. Magnesium also participates in aqueous complexation and secondary mineral precipitation (Table 1). The net Mg uptake by vegetation cycling is about 2.2×10^{-3} $mol/m^2/yr$ [*Herndon et al*., 2015], which is relatively small compared to the annual Mg outflux of about 5.0×10^{-2} $mol/m^2/yr$ from SSHCZO and is considered

Table 1. Key Reactions and Kinetic and Thermodynamic Parameters (All Values are From the Database EQ3/6 [*Wolery*, 1992] Unless Otherwise Noted)

Clay Dissolution [*Jin et al*., 2010]	$\log_{10} K_{eq}$	$\log_{10} k$ (mol/m^2/s)	Specific Surface Area (SSA, m^2/g)
$(Fe_{0.24}Mg_{0.38}Al_{0.38})_6(Si_{0.07}Al_{0.93})_4O_{10}(OH)_{8(s)}$ (chlorite) + $5.72H_4SiO_{4(aq)} + 4.56H^+ \leftrightarrow 1.44FeOOH_{(s)} + 2.28\ Mg^{2+} + 3Al_2Si_2O_5(OH)_{4(s)} + 11H_2O$	38.8	−12.5[a]	0.01 (1.1–7.7)[a]
$K_{0.77}(Si_{0.30}Al_{0.70})(Fe_{0.48}Mg_{0.07}Al_{0.45})AlSi_3O_{10}(OH)_{2(s)}$ (illite) + $0.91H^+ + 3.235H_2O \leftrightarrow 0.77K^+ + 0.48FeOOH_{(s)} + 0.07Mg^{2+} + 1.075Al_2Si_2O_5(OH)_{4(s)} + 1.15H_4SiO_{4(aq)}$	1.45	−14.1[b]	0.80 (40.6–215.0)[b]
Carbonate Dissolution and Secondary Precipitation			
$CaMg(CO_3)_{2(s)}$ (dolomite) $\leftrightarrow Ca^{2+} + Mg^{2+} + CO_3^{2-}$	−17.8[c]	−5.92[d]	0.01
$CaCO_{3(s)}$ (calcite) $\leftrightarrow Ca^{2+} + CO_3^{2-}$	−7.3	−6.65[e]	0.01
$MgCO_{3(s)}$ (magnesite) $\leftrightarrow Mg^{2+} + CO_3^{2-}$	−7.52[e]	−8.22[e]	0.01
Cation Exchange Reactions[f]			
$>XNa + H^+ \leftrightarrow >HX + Na^+$	2.40[f]		
$>X_2Ca + 2Na^+ \leftrightarrow >2NaX + Ca^{2+}$	0.50[f]		
$>X_2Mg + 2Na^+ \leftrightarrow >2NaX + Mg^{2+}$	0.50[f]		

[a]Brandt et al. [2003].
[b]Aylmore et al. [1970] and Köhler et al. [2003, 2005].
[c]Sherman and Barak [2000].
[d]Gautelier et al. [1999].
[e]Pokrovsky et al. [2005].
[f]Derived from Jin et al. [2010] using Vanselow convention, >X represents soil surface exchange sites.

negligible. The Mg concentrations therefore reflect the interplay between hydrological processes, solute transport, and geochemical reactions.

Based on geochemical measurements [*Brantley et al*., 2013c; *Jin et al*., 2010], different initial chemical conditions were assigned to soil waters and mineralogical composition in ridgetop (RT), midslope (MS), and valley floor (VF) (Table 2). The total inorganic carbon (TIC) in soil water was assumed to be similar to stream water and was calculated based on measured alkalinity and pH in stream water (ranging from 0.05 to 0.73 meq/L) [*Brantley et al*., 2013d]. We tuned values of clay surface area and cation exchange capacity (CEC) to reproduce measured stream and soil water [Mg].

Table 2. Initial Soil Water Chemistry and Mineral Compositions in Different Locations in SSHCZO (Mapped in Figure 2d)

Chemical Species	Ridgetop (RT)	Midslope (MS)	Valley Floor (VF)	Ways Obtained
Elemental Species (mol/L Except for pH)[a]				
pH	4.56	4.48	4.70	Measured
Magnesium	2.49×10^{-5}	5.41×10^{-5}	5.61×10^{-5}	Measured
Calcium	5.22×10^{-5}	4.97×10^{-5}	8.49×10^{-5}	Measured
Iron	5.80×10^{-7}	2.76×10^{-7}	4.32×10^{-7}	Measured
Chloride	3.69×10^{-5}	3.12×10^{-5}	3.93×10^{-5}	Measured
Silicon	8.72×10^{-5}	9.97×10^{-5}	1.13×10^{-4}	Measured
Potassium	2.19×10^{-5}	1.52×10^{-5}	2.33×10^{-5}	Measured
Sodium	1.90×10^{-5}	1.85×10^{-5}	2.67×10^{-5}	Measured
TIC	2.80×10^{-1}	2.80×10^{-1}	2.80×10^{-1}	Estimated[b]
Mineral Volume Fraction (m^3/m^3)[c]				
Illite	2.30×10^{-1}	2.18×10^{-1}	3.30×10^{-1}	Measured
Chlorite	5.59×10^{-2}	5.42×10^{-2}	5.41×10^{-2}	Measured
Kaolinite	$2,15 \times 10^{-2}$	2.29×10^{-2}	1.21×10^{-2}	Measured
Quartz	$4,97 \times 10^{-2}$	5.07×10^{-1}	3.94×10^{-1}	Measured
Calcite	4.90×10^{-4}	8.10×10^{-4}	2.03×10^{-3}	Model assumption[d]
FeOOH	0	0	0	Measured
Cation exchange capacity (CEC) ($\times 10^{-5}$ eq/g)	3.9 ($\pm$0.5)	4.0 ($\pm$0.5)	6.4 ($\pm$0.7)	Measured[e]
	5.0	4.0	6.0	Tuned

[a]Soil water chemistry data from *Brantley et al*. [2013c].
[b]Alkalinity was measured in stream water. We assumed as an initial guess that the soil water had similar alkalinity as stream water and we used pH and alkalinity measured in stream water to estimate TIC.
[c]Soil mineral composition data from *Jin et al*. [2010].
[d]Calcite was not observed in field samples. The model includes calcite to allow the possible precipitation of calcite when conditions allow.
[e]CEC values were measured previously for SSHCZO soils [*Jin et al*., 2010].

2.6. Model Setup

The code generates unstructured grids based on Delaunay triangulation, considering constraints related to river network, watershed boundary, elevation contours, vegetation, and geology [*Bhatt et al*., 2014]. Grids close to rivers and steep areas are typically small and those in flat, less dynamic areas are large. A total of 535 prismatic land elements and 20 stream segments were used for SSHCZO. PIHMgis, a tightly coupled GIS interface to PIHM, was used to set up the domain with mesh sizes varying from 10 to 100 m. The data infrastructure HydroTerre Data System (http://www.hydroterre.psu.edu) harvests, aggregates, and preprocesses essential terrestrial data from federal agencies (e.g., NED and NLCD) [*Bhatt et al*., 2014]. The time step in Flux-PIHM was set to one minute. The maximum time step for the RT module was set to five minutes. In this work, it takes 20–30 h of CPU time on an Intel® Xeon® CPU E5-2670 @ 2.60GHz for 2 years of simulation (2008–2009). The first year (2008) was used as a spin-up, which was run until steady state to avoid unphysical process representation. Unphysical representation can occur if, for example, the initial [Mg] is too low or too high for the natural systems to actually maintain. In such cases, the watershed could undergo unrealistic Mg accumulation or release before reaching "steady state." Model runs with different sets of parameters require different spin up time, which we manually adjust.

3. Model Calibration, Validation, and Model Data Comparison

3.1. Model Calibration and Performance Criteria

Data in April–May 2009 were used for calibration to estimate parameters that reproduce data. Data from June to December 2009 were used for validation, where the model prediction was compared to data to evaluate the goodness of simulation results. Note that although we used the same general-purposed code RT-Flux-PIHM for Cl and Mg, the processes included are fundamentally different: Cl does not participate in any reactions while Mg is involved in clay dissolution, ion exchange, and aqueous complexation. To produce Cl data, the deep groundwater influx was tuned; to produce Mg data, the clay surface area and the cation exchange capacity were calibrated. Here we use two statistical measures for the quantification of model performance: the Nash-Sutcliffe efficiency (NSE) and the Percent bias (PBIAS). As discussed in *Moriasi et al*. [2007], for monthly data and model comparison, a model is considered satisfactory if NSE $>$ 0.50 and if PBIAS $\leq \pm$70% for N and P. We assume similar standards for Cl and Mg as N and P.

The NSE quantifies the relative magnitude of residual variance of modeling output compared to those of measurements [*Nash and Sutcliffe*, 1970]. It has been widely used for performance evaluation of hydrological models. It has also been criticized for oversensitiveness to extreme values/outliers and exclusion of observation uncertainty [*Legates and McCabe*, 1999]. Here we use the modified NSE equations to take into account of the measurement uncertainty [*Harmel and Smith*, 2007], which is often large in field data. The modified NSE replaces the original error term e_i (model and observation difference of ith observation and model output pair) by a modified error term eu_i that includes measurement uncertainties based on the following:

$$eu_i = \begin{cases} 0, & UO_i^{lower} \leq Y_i^{sim} \leq UO_i^{upper} \\ UO_i^{lower} - Y_i^{sim}, & Y_i^{sim} \leq UO_i^{lower} \\ UO_i^{upper} - Y_i^{sim} & Y_i^{sim} > UO_i^{lower} \end{cases} \tag{3}$$

where Y_i^{obs} and Y_i^{sim} are the ith observation and modeling output, respectively; UO_i^{lower} is the lower uncertainty boundary $\left(=Y_i^{obs} - \frac{PER_i \times Y_i^{obs}}{100}\right)$ and UO_i^{upper} is the upper uncertainty boundary $(=Y_i^{obs} + \frac{PER_i \times Y_i^{obs}}{100})$ for the ith measured data point, with PER being the probable error range ($\pm$%) in measurement uncertainty calculated from observation data. The NSE can then be calculated as follows:

$$NSE = 1 - \frac{\sum_{i=1}^{n} (eu_i)}{\sum_{i=1}^{n} (Y_i^{obs} - Y^{mean})^2} \tag{4}$$

where Y^{mean} is the mean observation and n is the total number of observations.

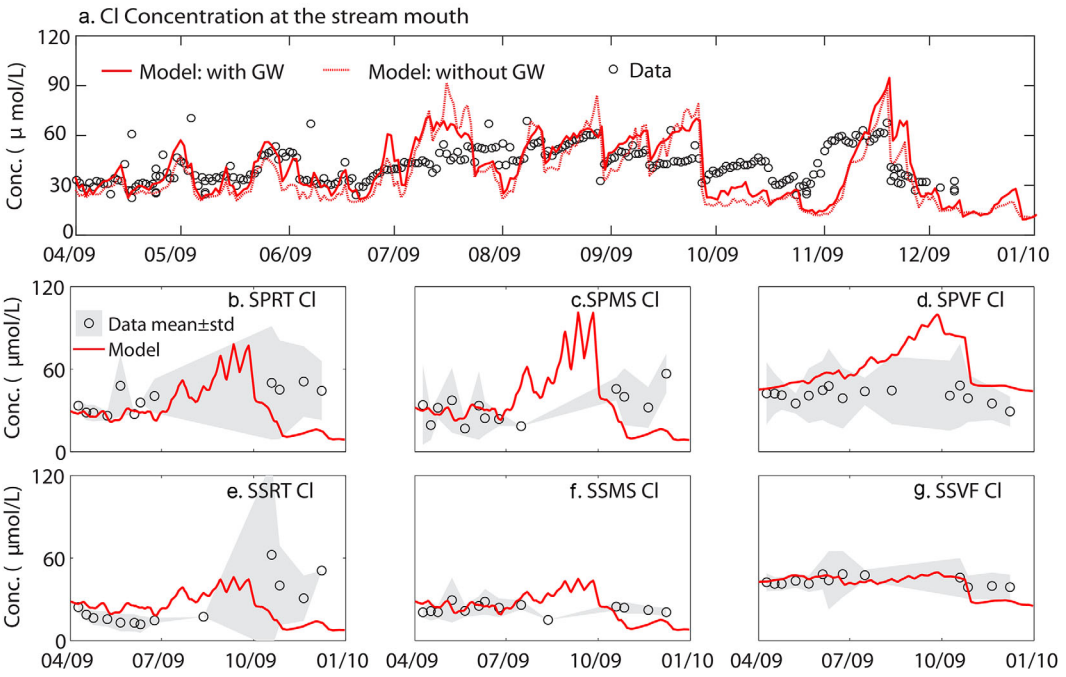

Figure 5. Temporal evolution of [Cl] data (averaged over multiple samples) and modeling output from 1 April to 31 December 2009. (a) Concentrations at the stream mouth; (b–g) concentrations in soil water in six lysimeter sites (Figure 3). Grey areas indicate ±one standard deviation for measured soil water chemistry.

The Percent bias (*PBIAS*) measures the deviation of model output from corresponding observations [*Gupta et al.*, 1999]:

$$PBIAS = \frac{\sum_{i=1}^{n}(Y_i^{obs} - Y_i^{sim})}{\sum_{i=1}^{n} Y_i^{obs}} \times 100\% \quad (5)$$

A PBIAS value of 0.0 indicates no deviation; positive and negative values indicate model underestimation and overestimation, respectively.

3.2. Chloride

With the already tuned hydrological parameters in Flux-PIHM [*Shi et al.*, 2013], the Cl influx from deep groundwater is the only tuning parameter for reproducing Cl data. As shown in Figure 5a, [Cl] in stream water gradually increases from spring to summer when the watershed becomes drier, and then gradually decreases until November when the watershed becomes wetter. On 5 October, a snowstorm hits Shale Hills followed by a heavy rain on the 24th. The big precipitation event flushes the trapped Cl, leading to a [Cl] peak in stream water in November. This peak appears in both measured and simulated data. The time lag between storm and peak in discharge is very short in the simulation compared to the data, probably due to the relatively simple representation of snow physics that leads to much faster snow melt than in reality [*Kumar et al.*, 2009]. As shown in Figures 5b–5g, evapotranspiration increases and draws more water in the summer so that Cl becomes concentrated in soil water. This is more pronounced in the planar slope than in the swales, where water converges and flushes out Cl even under dry conditions [*Qu and Duffy*, 2007]. RT-Flux-PIHM reproduces the magnitude of [Cl] at the stream mouth and in soil water (Figure 5). The model predicts a [Cl] peak during summer in all locations except the South Slope Valley Floor (SSVF); soil water data however are not available under the dry conditions in the summer.

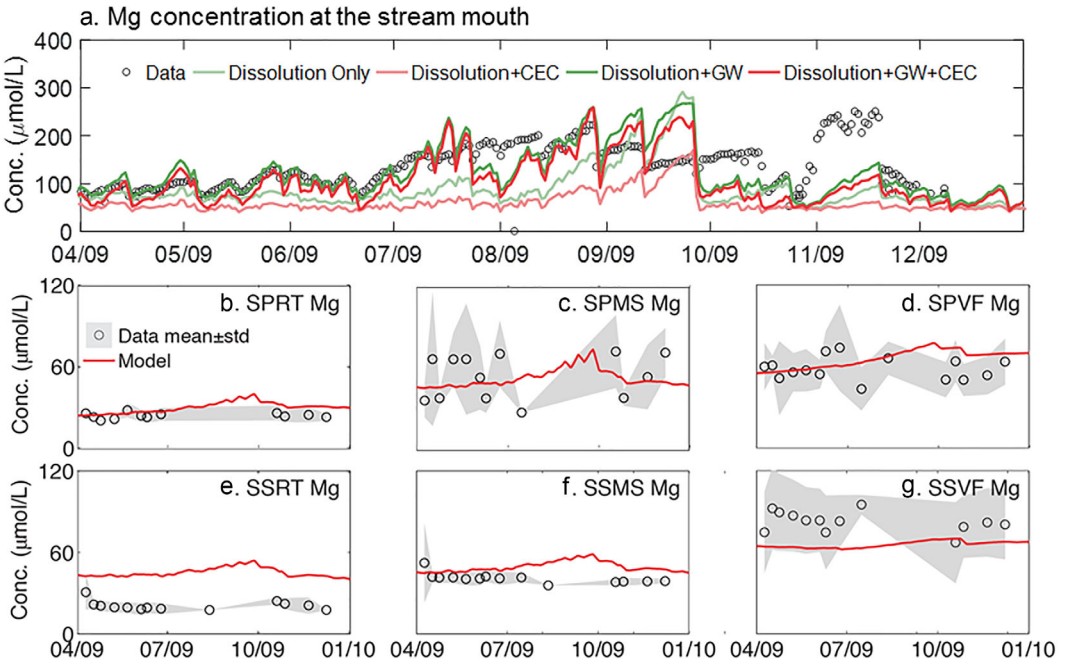

Figure 6. Temporal evolution of measured and modeled [Mg] in (a) stream water (average over multiple samples) in four scenarios: Dissolution-Only, Dissolution + CEC, Dissolution + GW, Dissolution + GW + CEC (best fit); (b–g) soil water in different sampling locations, including the three south planar sites (SPRT, SPMS, SPVF) and three south swale sites (SSRT, SSMS, SSVF). Grey areas indicate ±one standard deviation for measured soil water chemistry.

3.3. Magnesium

In reproducing Mg data, we directly used the deep groundwater influx tuned for Cl data and measured Mg groundwater concentrations. The clay specific surface areas (SSA) were tuned using literature values as the initial guess. The equilibrium constants for ion exchange reactions were estimated from measurements assuming soil water and soil surface were at equilibrium [*Jin et al*., 2010]. Measured cation exchange capacity (CEC, [eq/g]) [*Jin et al*., 2010] was used first and then tuned to reproduce soil water concentration. The soil CEC that reproduced data (Table 2) is close to the mole-fraction-weighted CEC values estimated using mole fractions of chlorite and illite in soils and their corresponding CEC values of 0–10 $\times$ 10^{-5} eq/g and 10–40 $\times$ 10^{-5} eq/g in literature, respectively [*Weaver*, 1989].

Of all parameters, model output depends most strongly on clay surface area. The values of 0.01 and 0.86 m^2/g for chlorite and illite used in the model are about 2 orders of magnitude lower than the laboratory-measured Brunauer-Emmett-Teller (BET) surface areas for chlorite [*Brandt et al*., 2003] and illite [*Aylmore et al*., 1970]. The product of kinetic rate constant and the surface area for chlorite (m^2/m^3) (6.5 $\times$ 10^{-10} $mol/m^3/s$) is close to rates estimated from field data (7.6 $\times$ 10^{-10} $mol/m^3/s$) [*Jin et al*., 2011a]. The specific surface area used here reflects the effective surface area that are truly reacting [*Li et al*., 2014; *Moore et al*., 2012; *Salehikhoo and Li*, 2015; *Wen et al*., 2016]. The fact that we need to lower SSA to reproduce data reflects the commonly observed laboratory-field rate discrepancy [*White and Brantley*, 2003]. In addition, FeOOH or organic matter could be armoring mineral surfaces. In effect, the effective surface area that interacts with flowing water is much lower than the surface area of clay powders measured by BET method.

Figure 6a compares four model simulation cases: the base case that reproduces data with dissolution, cation exchange, and deep groundwater influx (Dissolution + GW + CEC), a dissolution-only case (Dissolution-Only), dissolution and cation exchange without deep groundwater influx (Dissolution + CEC), a case with dissolution and deep groundwater influx without cation exchange (Dissolution + GW). Comparison between Dissolution-Only and Dissolution + CEC cases shows much more variation in Dissolution-Only, reaching twice as high concentrations as those in Dissolution + CEC in mid-September. The GW introduces additional Mg mass into the stream, as shown in the Dissolution + GW and Dissolution + CEC + GW compared to their corresponding counterparts without GW. The base case with all processes produces modeling

Table 3. Measures of Data-Model Comparison for Cl and Mg in Stream and in Soil Waters

Element	Acceptable Range[a]	Stream	SPRT	SPMS	SPVF	SSRT	SSMS	SSVF
Cl								
NSE (PER, %)	[0.5 1]	0.62 (19.5%)	0.78 (36.5%)	0.46 (30.2%)	−18.50 (17.4%)	0.63 (39.1%)	−0.30 (21.6%)	−2.89 (22.5%)
PBIAS (%)	≤±70	9.37	31.6	−3.83	−48.1	17.2	9.70	36.3
Mg								
NSE (PER, %)	[0.5 1]	0.39 (14.6%)	0.63 (18.3%)	1.00 (35.3%)	0.84 (26.9%)	−28.9 (18.0%)	−0.92 (11.4%)	0.087 (30.3%)
PBIAS (%)	≤±70	4.47	−2.35	1.13	0.14	−99.30	−11.70	36.80

[a]The acceptance range based on *Moriasi et al.* [2007] for monthly comparison, a model is considered satisfactory if NSE > 0.50 and if PBIAS ≤ ±70% for N and P. We assume similar standards for Cl and Mg as N and P. The PER (%) values in the parentheses are the probable error range in measurement uncertainty calculated from observation data. Note that although we use monthly criteria, the model-data comparison for stream water [Cl] and [Mg] is daily. For monthly model-data comparison, the NSE and PBIAS values are 0.86 and 10.5 for Cl in stream water, respectively; NSE and PBIAS values are 0.66 and 4.34 for Mg in stream water, respectively.

output that is closest to the data. Also note that the best fit for both Cl and Mg has deep groundwater component.

3.4. Model Data Discrepancy

Table 3 indicates that the model performance is acceptable for some locations however not all locations. As indicated in Figures 5a and 6a, the model output of stream concentrations has more variation than in the data over July–September, indicating ion exchange does not necessarily reproduce the full degree of chemostasis during this period. Also, at the end of October, the data show flushing behavior with large increase in stream [Mg], which the model does not capture. In fact, most model errors come from the period of mid-September to early November. Excluding this period in NSE calculation increases NSE values to 0.788 and 0.818, respectively. Note that the [Cl] and [Mg] data-model comparison in Table 3 are daily comparison, not monthly. For monthly model-data comparison, the NSE and PBIAS values are 0.86 and 10.5, respectively, for Cl in stream water; NSE and PBIAS values are 0.66 and 4.34, respectively, for Mg in stream water. The model does not reproduce soil water chemistry of the south swale sites well with NSE values out of the acceptable range.

The discrepancy between model and data for Cl and Mg may be largely due to the complexities of processes and watershed characteristics. Although the model explicitly takes into account surface characteristics including topography, land cover, soil type, the model does not consider spatial heterogeneities at the vertical direction because such vertical structure is largely not characterized. As supported by spatially explicitly water chemistry and isotope data [*Jin et al.*, 2011a; *Thomas et al.*, 2013]. The subsurface has been observed to be highly heterogeneous with preferential flow path leading to zones of "high flow" and "low flow." In addition, soil water chemistry is measured at small spatial scales with water samples of milliliters. The model has grid sizes from 10 to 100 m such that the model output represents averaged values at the grid scale. Such discrepancy in spatial scales between model and measurements can contribute to differences between observations and model output. Geochemical processes also tend to be "local" and are sensitive to local conditions. The representation of geochemical properties, including mineral surface area and ion exchange, is based on a few measurements that coarsely define different parts of the watershed (ridgetop, midslope, and valley floor). Such representations can also lead to observation-model discrepancies.

4. Controls of Hydrogeochemical Dynamics

4.1. Chloride

Figure 7 shows simulated spatial profiles of water and [Cl]. The valley floor and swales are areas of gravity-driven convergent flow. In spring and winter, [Cl] is relatively low because large hillslope areas are connected to the stream, allowing Cl export out of the watershed. From spring to summer, the depth to the water table (DWT) increases as the watershed gradually loses water to high ET. In the summer, discharge is very low because only a small proportion of the watershed is connected to the stream (Figure 7b). As a result, most Cl is trapped in pockets of immobile soil waters that are not "connected" to the stream, leading to elevated soil water concentrations that are more than one order-of-magnitude higher than throughfall concentrations (∼5 μmol/L) (Figure 7d). This is particularly interesting because Cl is considered nonreactive and its concentrations are expected to be constant. The model however is telling a different story. Although

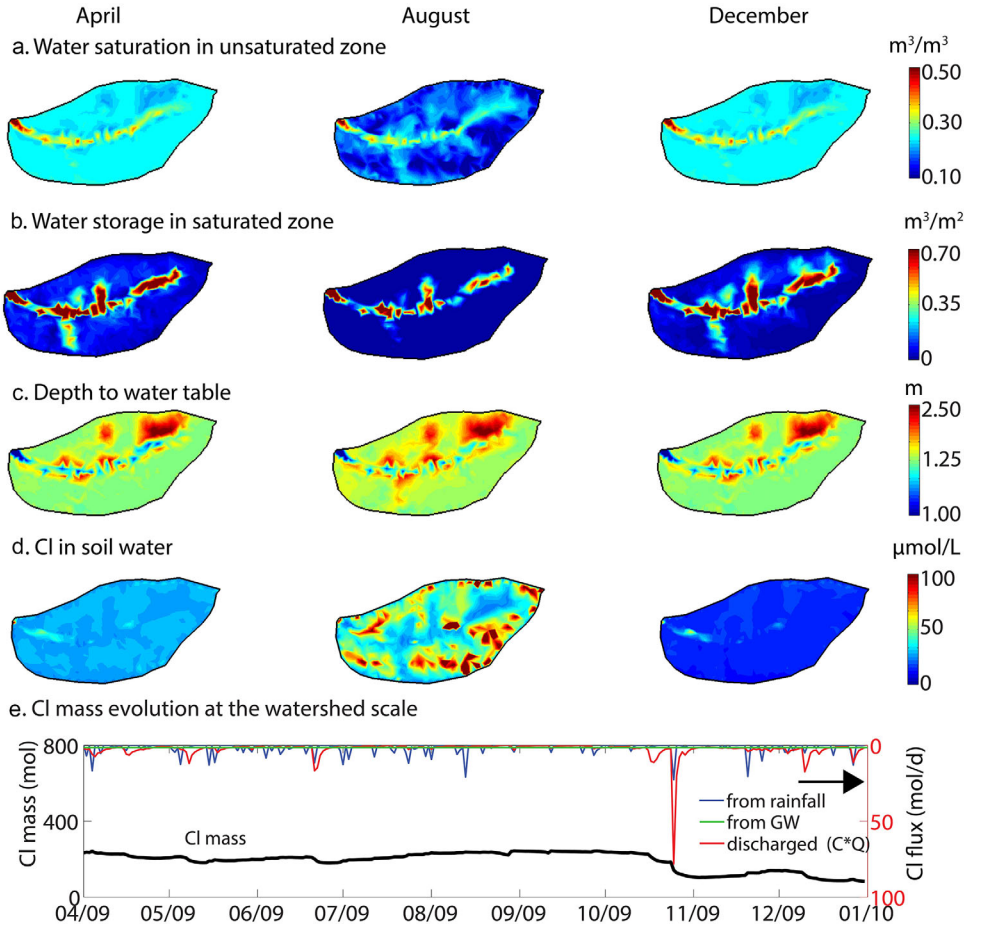

Figure 7. Spatial profiles on 1 April, 1 August, and 1 December in 2009. (a) Water saturation in the unsaturated zone (m^3/m^3); (b) water storage h_g in the saturated zone (m^3/m^2); (c) depth from ground surface to water table (DWT) (m); (d) [Cl] in soil water (μmol/L) (calculated as a water-volume-weighted average over the saturated and unsaturated zones); (e) total Cl mass (calculated as the summation of soil water volume times [Cl] in individual grid blocks over the entire watershed), plotted along with daily chloride influx from rainfall and out-flux (calculated as $C_D \times Q_D$) (mol/d).

Cl does not react with soil minerals, its soil concentrations vary spatially and temporally because of the water dynamics: at times and locations with abundant water, more Cl is flushed out, leading to lower [Cl] in "old," preevent soil water; in contrast, dry conditions arising from high ET elevate [Cl] in soil water, driving the concentrations to levels that are much higher than those in rainfall.

The watershed mass balance is shown in Figure 7e. The total Cl mass is the summation of soil water volume times concentration in each prismatic element. The Cl input is the product of rainfall volume and [Cl], and the output is the discharged Cl ($C_D \times Q_D$). It is important to note that although stream [Cl] vary only from 25 to 70 μmol/L (Figure 5a), the mass fluxes ($C_D \times Q_D$) vary by orders of magnitude because of the orders of magnitude variation in discharge. The change in Cl mass is largely determined by the mass balance between the rainfall input and discharge output. Low discharge and low connectivity in the summer result in negligible Cl export and therefore Cl accumulation in the watershed. Intense rainfall and snowfall in late October mobilize trapped Cl, leading to a drop of ~50% in total Cl mass (Figure 7e). Model results show that even after this event, large Cl masses remain in the watershed, indicating Cl storage in soil. The increase of Cl concentrations with higher ET and lower recharge is well documented and serves as the basis for the chloride mass balance method for estimating groundwater recharge [*Rice and Hornberger*, 1998; *Semenov and Zimnik*, 2015].

4.2. CQ Relationship

As shown in Figure 8a, both Cl data and model output exhibit chemostatic behavior. The model predictions at higher discharges are lower than data because of the underestimation of stream [Cl] in the late October

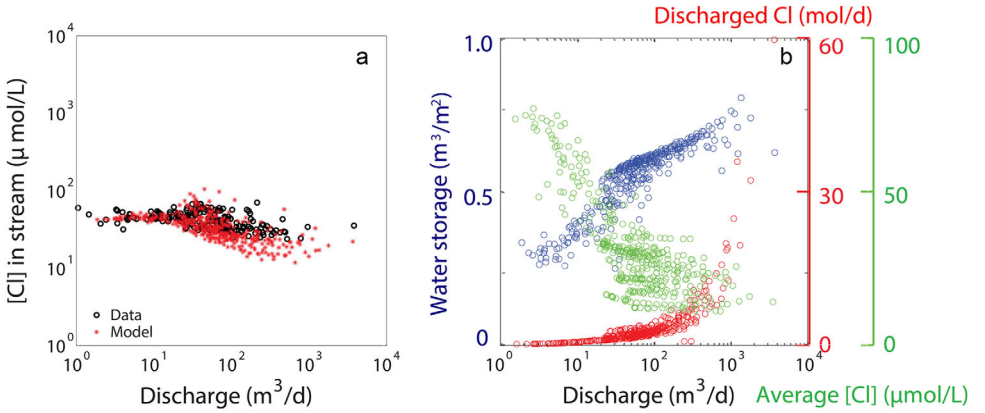

Figure 8. (a) Cl CQ relationships. The power law CQ slopes are −0.030 (±0.006) and −0.101 (±0.006) for data and model output, respectively. (b) Total water storage (in saturated and unsaturated zones, normalized by land surface area), Cl outflux (discharged Cl), and average Cl in soil water over the entire watershed (average [Cl]) as a function of discharge.

snow/heavy rain events (Figure 5a). As shown in Figure 8b, discharge increases by 3 orders of magnitude while water storage increases only by approximately a factor of 3, which is further accompanied by about a factor of 2 decrease in average [Cl]. Average [Cl] in soil water does not decrease as much as water increase because (1) the incoming rainwater contains Cl and (2) mobilization of trapped Cl in soil counteract dilution effects induced by higher water content. Nonetheless, mass export of Cl increases corresponding to orders of magnitude increase in discharge.

4.3. Magnesium

4.3.1. Mg Processes

Water storage influences clay dissolution by controlling the wetted surface area of clays in the shallow regolith (equations (1) and (2)). As shown in Figure 9a, chlorite dissolves faster in swales and valley floor where water is abundant and connected to the stream. Watershed-average dissolution rates decrease by about half in the summer. The chlorite dissolution rate calculated from the model based on the daily mass change of chlorite averaged over the year 2009 is about 1.70×10^{-10} mol/m^3/s, which is close to the rate of 1.90×10^{-10} mol/m^3/s estimated from soil profiles [*Jin et al.*, 2010]. Although not shown here, illite dissolution rates vary in similar spatial and temporal patterns as that of water storage. Groundwater influx has a larger impact on stream chemistry from July to September, which is consistent with field observations [*Jin et al.*, 2014; *Thomas et al.*, 2013]. No carbonate precipitation was observed in the simulation.

It has been speculated that cation exchange regulates [Mg] in soil water and sets the lower limit of [Mg] in stream water [*Clow and Mast*, 2010; *Herndon et al.*, 2015]. As shown in Figures 9b and 9c, [Mg] in soil water is relatively constant over time. In spring and winter, [Mg] is only slightly lower than those in the summer. The [Mg] on exchange sites is highest in the valley floor (Figure 9c). This is because convergent water flow continuously brings Mg mass fluxes from the upslope, which is consistent with the observations that [Mg] on the exchange sites in the south planar valley floor (SPVF) are higher than in ridge top (SPRT) and middle slope (SPMS) [*Jin et al.*, 2010]. Predicted [Mg] on exchange sites in general agrees with measured data except that the model underestimates [Mg] on exchange sites in the valley floor.

Concentrations of Mg in soil water do not increase as much as Cl during the summer primarily because cation exchange acts as a buffering mechanism. Figures 9d and 9e show that clay dissolution is slower due to lower water content and lower wetted surface area in the summer. Effluxes of Mg are also lower, leading to total Mg mass increase (in the form of dissolved Mg in soil water and Mg associated with CEC). This is similar to Cl except that the exchange sites store more than an order-of-magnitude higher mass and therefore reduces the spatial and temporal variation of [Mg]. In late October, precipitation events flush out 2.1% of the total Mg mass, compared to about 50% mass drop of Cl. In contrast to Cl, Mg mass remains mostly on the exchange sites even after the large precipitation event because the cation exchange equilibrium limits Mg that can come off the exchange sites. Overall, the annual influx of Mg from dry and wet deposition

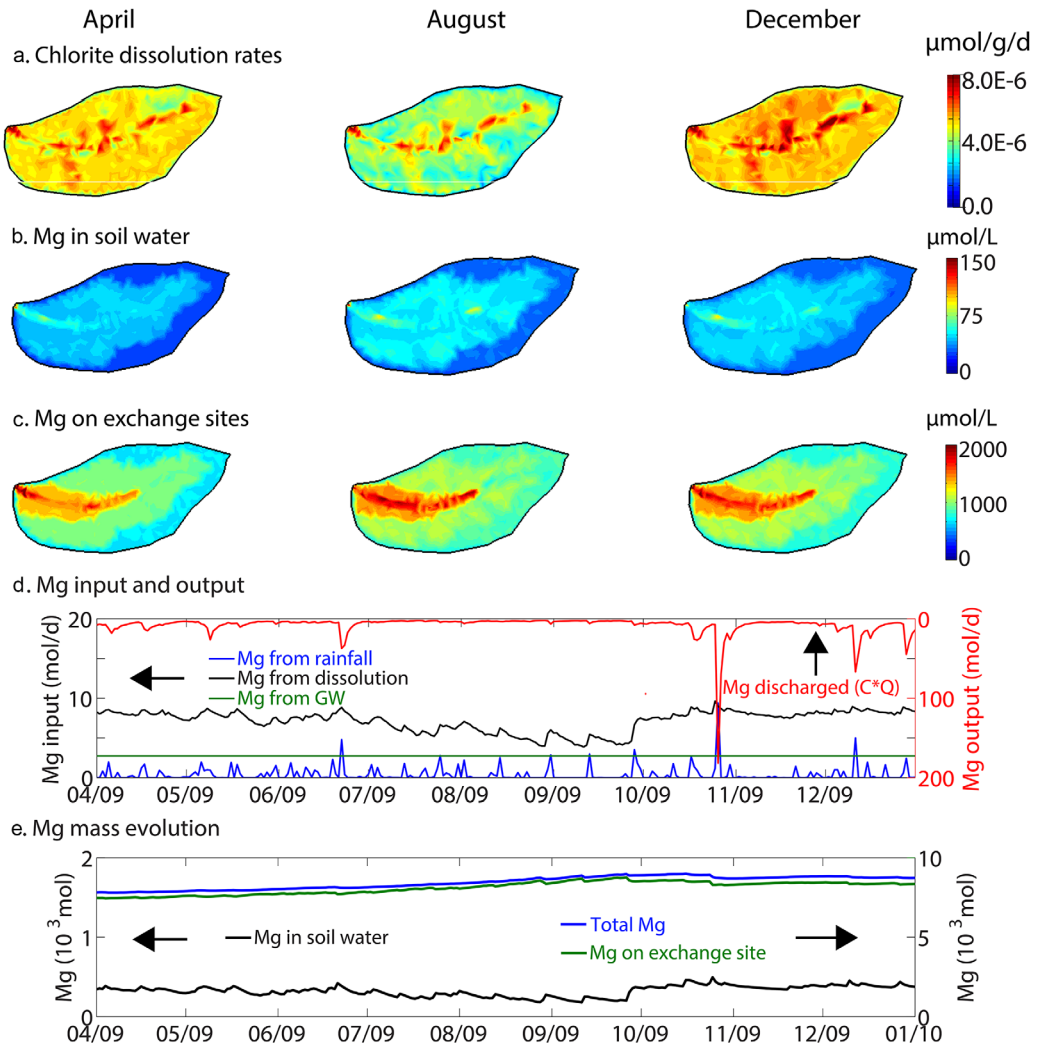

Figure 9. Model output for spatial distribution of (a) chlorite dissolution rate (μmol/g/d) on 1 April, 1 August, and 1 December 2009 (rates in each grid block were summed up rates (mol/d) in the unsaturated and saturated zones and normalized by total mineral mass); (b) [Mg] in soil water (μmol/L water); (c) [Mg] on exchange sites (μmol/L water); (d) daily input from rain water, clay dissolution, and groundwater, and effluxes as stream discharge ($C_D \times Q_D$, mol/d); and (e) evolution of Mg mass in soil water and on exchange sites over the entire watershed. Total Mg is the sum of Mg mass in soil water and on exchange site. The exchange sites store an order-of-magnitude more Mg mass compared to soil water.

(117 mol/yr) is a negligible 2.5% of the total Mg outflux (~4700 mol/yr). Clay dissolution accounts for 77.7% (3648 mol/yr) of this outflux, while the groundwater influx (~1000 mol/yr) contributes 21.3%.

The clay dissolution and water content are strongly coupled at the watershed scale (Figure 10). As discharges increase by more than 3 orders of magnitude, V_w increases by a factor of about 3, which is accompanied by an increase of A_w and R by a factor of about 2.1. Faster clay dissolution releases Mg quickly, therefore counteracting the dilution effect brought about by higher V_w. This synchrony between increases in water storage, wetted surface area, and dissolution rates maintains a relatively constant [Mg] in soil water. Figure 10 also indicates a clear division at a discharge value of about 20 m^3/d. Concentrations and dissolution rates are more sporadic and scattered at discharge $<$20 m^3/d and are much more consistent at discharges $>$20 m^3/d, indicating 20 m^3/d as a critical value that divides dry and wet conditions. Under dry conditions, soil [Mg] decreases quickly as discharge increases, likely because the watershed is not connected yet. At discharge above 20 m^3/d, the watershed is much more connected and [Mg] in soil water is controlled more by the synchronous change in dissolution rates and water content as the watershed connects.

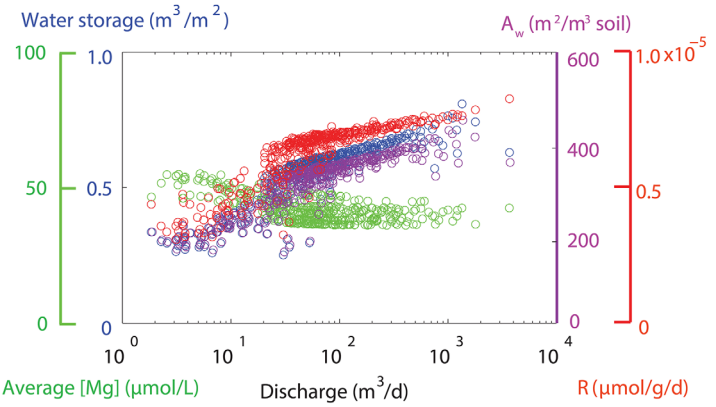

Figure 10. Watershed-scale quantities versus discharge: water storage V_w (summation of water storage in saturated and unsaturated zones in each prismatic element, normalized by land surface area), average [Mg] in soil water (total Mg mass in soil water divided by total soil water volume), wetted surface area A_w (summation of total surface area multiplied by water saturation in saturated and unsaturated zones in each prismatic element, normalized by total soil volume), chlorite dissolution rate R (total mass loss rates of chlorite over the entire watershed). The dissolution rates R increase at the same rate as A_w, leading to similar increase in dissolved Mg, as indicated by essentially the same slopes of A_w, V_w, and R versus discharge. The increase in dissolved Mg mass is counterbalanced by the larger total water storage, leading to relatively constant average [Mg] under different discharge conditions.

4.3.2. CQ Relationships

In Shale Hills where stream discharge varies over almost 3 orders of magnitude, the stream discharge [Mg] varies by a factor of 3 at maximum. The power law slopes (b) are −0.056 (±0.005) and −0.046 (±0.004) for the data and for the best fit model (represented as the 1X case with GW in Figure 11c), respectively. As discussed in Figure 10, Mg chemostasis is best explained by synchronous responses of water storage, clay dissolution rates, and subsurface lateral flow to changing hydrological conditions. Figure 11 compares cases of varying SSA and CEC under conditions with and without deep groundwater influx. In each case, only one parameter is changed while all other parameters are kept the same as the best fit base case (1X SSA and 1X CEC). In cases without deep groundwater (NO GW), stream [Mg] changes as surface area changes, although the b values vary narrowly between −0.02 and −0.08 (Figure 11a); varying CEC also has negligible impacts on the CQ slope (Figure 11b). With GW, the 5X CEC case exhibits some dilution behavior with a slope of −0.25 ((Figure 11d) because soil water [Mg] is lower under high CEC conditions, essentially increasing the impact of constant GW influx on stream discharge [Mg] relative to lateral flow.

The deep groundwater influx affects CQ relationships by introducing an additional Mg source. Under low discharge conditions, the deep groundwater influx dominates Mg effluxes into stream, leading to relatively constant stream concentrations under all parameter conditions (Figures 11c and 11d). In the low SSA case (Figure 11c), clay dissolution rates are low and the primary Mg influx into the stream is the constant groundwater influx that is not as responsive to hydrological conditions. This leads to a CQ relationship demonstrating more of a dilution trend (decreasing concentration as discharge increases, more negative b values, green dots in Figure 11c). The CQ power law slope becomes progressively steeper as the SSA values decrease from 5X to 0.2X with groundwater influx becoming the increasingly dominant Mg mass influx into the stream. As summarized in Figure 12, the NO GW cases exhibit chemostasis with b values deviating less than 0.20 from zero. With GW cases, however, CQ relationships change from slight dilution (b value of −0.35) to chemostatic b value of 0.0 as SSA values increase from 0.2X to 5.0X of the base case, respectively.

5. Discussion

5.1. Old Water Versus New Water

The model predicts that the "new water" or "event water" coming from rainfall contributes a small percentage to the stream discharge through surface runoff Q_S (typically <20%) (Figure 4b). In contrast, more than 70% of the stream discharge comes from the subsurface lateral flow Q_L in the saturated soil zone. This dominance of subsurface lateral soil water echoes observations in sprinkling experiments that about 60–90% of total runoff is from subsurface flow [*Anderson et al.*, 1997]. Other studies also concluded that more than 50% of "preevent" soil water or groundwater contributes to stream flow in 55 small-sized and medium-sized basins of different characteristics [*Buttle*, 1994].

During the rainfall events, new rainwater infiltrates and increases soil water content, therefore forming lateral flow that rapidly mobilizes the old water into the stream [*Kirchner*, 2003]. Figure 8 and 10 suggest a

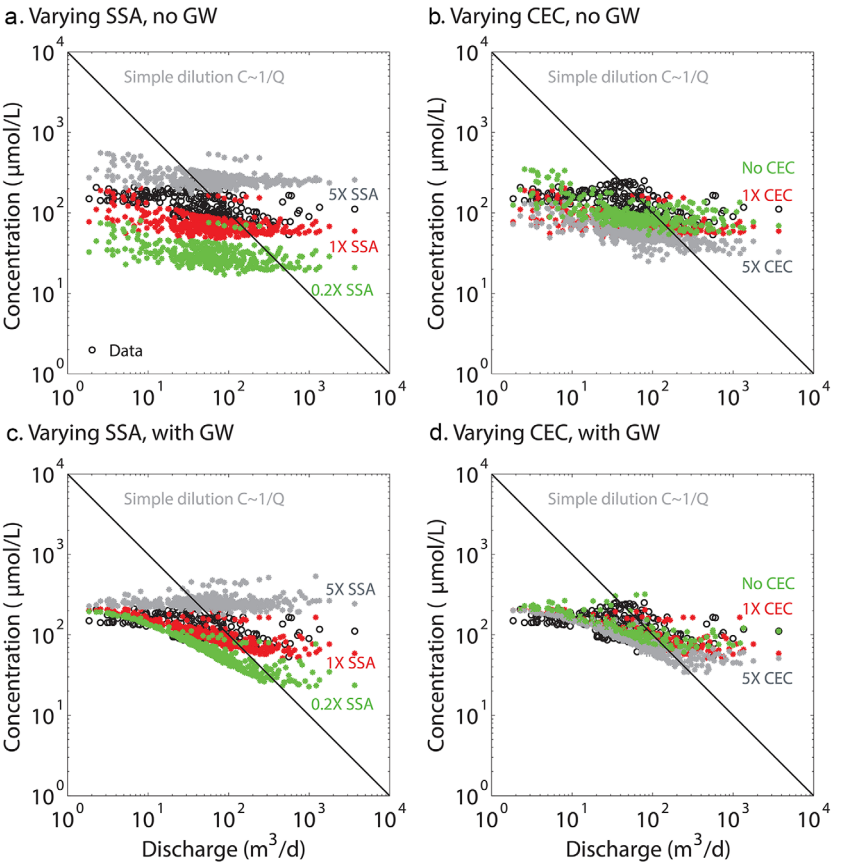

Figure 11. Sensitivity of Mg CQ relationships. (a) Varying specific surface area (SSA) without groundwater influx (GW); (b) varying cation exchange capacity (CEC) without GW influx; (c) varying SSA with GW; and (d) varying CEC without GW influx. The red dots are output from the best fit model with GW, SSA, and CEC in the base case (1X SSA and 1X CEC).

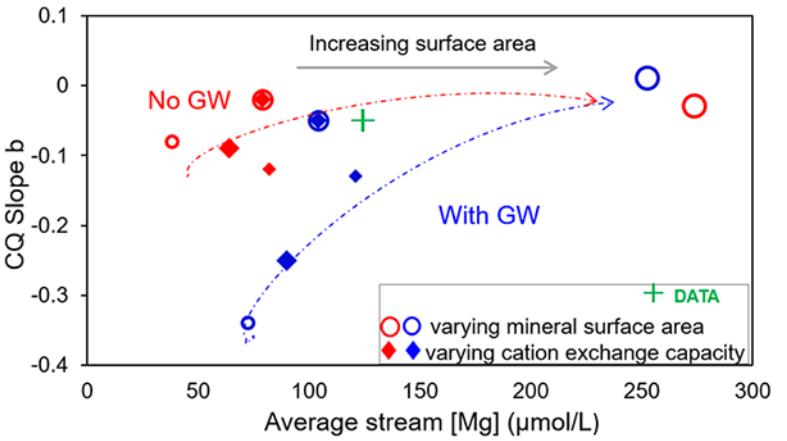

Figure 12. The CQ power law slope b and stream discharge [Mg] (averaged over all discharge conditions) for cases in Figure 11. The symbol size corresponds to the magnitude of varying parameters. When no deep groundwater is present (NO GW), all cases exhibit chemostasis with b values within 0.20 from zero. With the presence of deep groundwater (With GW), CQ relationships change from slight dilution (b values as low as −0.35) to chemostasis with b values close to zero. This is because clay dissolution becomes an increasingly dominant contributor to the stream Mg as SSA increase. Slight dilution occurs only under conditions of small SSA or large CEC values so that the GW mass influx dominates over clay dissolution influx.

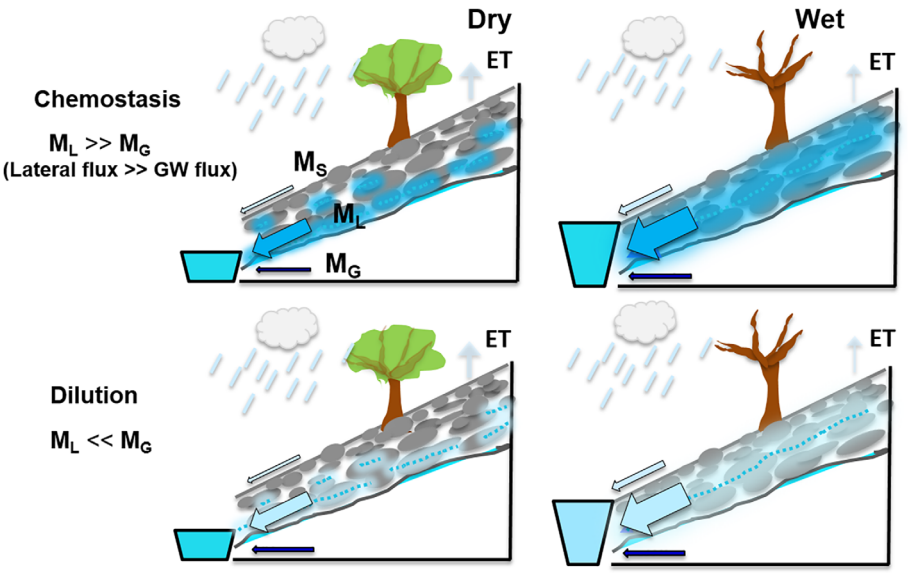

Figure 13. A schematic diagram of mechanisms for CQ behavior. The color gradient of arrows indicate increasing solute concentrations in fluxes from surface runoff (light) to deep groundwater flow (darker). Arrow size water represents magnitude of water fluxes. The mass flux M_S is from surface runoff Q_S, M_L is from Q_L, and M_G is from deep groundwater influx Q_G. The M_S is negligible because Q_S and concentrations in Q_s are low. The M_L depends on clay dissolution/Cl mobilization rates and Q_L is responsive to surface hydrological conditions. (Top panel) When soil minerals have large surface areas, leading to the dominance of M_L, chemostasis occurs; (bottom panel) if soil mineral surface area is low and dissolution rates are low, M_G dominates mass flux, dilution occurs because M_G is relatively constant and not as responsive to surface hydrological conditions.

critical discharge value of around 20 m^3/d before sufficient connection to the stream to mobilize old water. The new water also mixes with the old soil water and interacts with soil minerals. In doing so it modifies its composition. For the nonreactive Cl, its changes in concentrations primarily reflect the mixing with trapped Cl in immobile water pockets or dissolution from salt residues. For reactive solutes, their concentrations can be modified not only by mixing but also by their participation in soil-water interactions, which can lead to distinct responses to hydrological changes depending on specific types of reactions [*Kirchner*, 2003]. Although deeper groundwater, another type of old water with residence times longer than shallow soil water, can contribute to stream water all year long, its contribution is more dominant under dry conditions.

It is important to note that although in the model Cl reaches the whole watershed through wet deposition, not all Cl is exported out of watershed, especially under dry conditions when rainfall is not sufficient to form subsurface lateral flow. Under these conditions, the Cl accumulates with high salt concentrations, leading to high spatial variations in [Cl] (Figure 7) even though Cl is modeled as a nonreactive tracer. In fact, the spatial variation in [Cl] supports the speculation that "a continuum of stores of 'old' water, each with a different chemical signature, and these are mobilized in different proportions at high and low flow," [*Kirchner*, 2003]. This "accumulation" can possibly form salt residues in soil water and can act as a long-term Cl source, as Figure 7e implies. Interestingly, soil water [Mg] shows much less spatial variations due to the regulation of ion exchange on soil water concentrations.

5.2. Controls of CQ Relationships

With different waters contributing to the stream, solute mass fluxes (in the units of mass/time, not water fluxes) into the stream come from three major sources: M_S from Q_S, M_L from Q_L, and M_G from Q_G (Figure 13). For Mg, M_S is negligible because Q_S and [Mg] in rainwater are low (Figure 4b). The M_G is relatively constant and is mostly unresponsive to surface hydrological conditions. Values of M_L depend on clay dissolution and Q_L, both of which are responsive to changing hydrological conditions. In other words, clay dissolution rates increase responding to the water content increase through A_w, counteracting dilution effects brought about by large V_w and Q_L, therefore maintaining relatively constant stream concentrations, as shown for the case of $M_L \gg M_G$, (top row, Figure 13).

In this respect, Mg chemostasis is similar to Cl chemostasis. As indicated in Figure 7e, some Cl mass remains in the watershed even after the largest rainfall event, suggesting the potential formation of salt residues

during dry conditions, which can act as long-term Cl sources within the watershed in similar ways as soil minerals. The mobilization of trapped Cl mass grows proportionally to lateral soil flow, therefore maintaining relatively constant stream concentrations. Simulation results also suggest that when soil dissolution is low with small surface area or rate constants, the hydrologically unresponsive M_G can dominate stream mass flux so that dilution occurs as large rainfall brings in more water to dilute the constant M_G (bottom row in Figure 13). This happens in the case with 0.2X SSA and GW (green dots in Figure 11c).

Multiple hypotheses have been put forward to explain CQ chemostasis. End-member mixing analysis (EMMA) has long been used to explain CQ relationships [*Johnson et al*., 1969]. One can think of the process-based model here as a dynamic EMMA compared to those in literature that consider static composition of end-members [*Evans and Davies*, 1998]. The importance of hydrologically responsive clay dissolution supports the porosity-permeability-aperture model for explaining chemostatic behavior in *Godsey et al*. [2009], a key feature of which is the increasing surface area (and catchment-scale dissolution rates) responding to discharge increases. Interestingly, "biogeochemical stationary," or near constant annual average nutrient concentrations, has been observed in many intensively managed watersheds of differing size and attributes [*Basu et al*., 2011, 2010b]. This chemostasis of nutrients has been hypothesized to reflect large legacy nutrient sources from historical fertilizer applications. This may reflect similar presence of nutrient sources in agricultural lands as soil minerals in forest lands. Both are abundant and occur ubiquitously similar abundance as soil minerals discussed here [*Basu et al*., 2010a; *Thompson et al*., 2011].

Chemostatic behavior has been considered as caused by chemical equilibrium when the catchment length scale is longer than the equilibrium length scale [*Maher*, 2011]. The simulations here indicate that this is not the case in SSHCZO because clays dissolve under far-from-equilibrium conditions with the formation of secondary minerals. Our work here indicates that ion exchange plays a secondary role in the Mg chemostasis. Ion exchange buffers the system and controls stream discharge [Mg] at times of extreme hydrological conditions such as intense rainfall and very low discharge conditions. It also leads to CQ hysteresis in single rainfall events [*Bao et al*., 2017]. Its effect on CQ relationship however is relatively limited compared to that of clay dissolution and GW influx. The fact that ion exchange plays a minor role in chemostasis is consistent with chemostatic behavior observed for Si [*Godsey et al*., 2009], which does not exchange on surface sites.

The role of the deep groundwater influx is highlighted here. The source of Mg in deep groundwater is still dissolution however it is dictated by minerals in the deep subsurface that are accessed close to the stream. There is strong field evidence that deep groundwater may come into direct contact with the stream through fractures in shale-bedrock watersheds like SSHCZO [*Brantley et al*., 2013a; *Jin et al*., 2014] or in Plynlimon, Wales [*Neal et al*., 1997a, 1997b]. It has been estimated that in Plynlimon, deep groundwater influx contributes as much as 25% of stream flow [*Neal et al*., 1997b]. Whether such groundwater influx becomes the dominant source of cations in the stream not only depends on groundwater flow rate but also on their concentrations of cations relative to soil water concentrations.

In general, simulation results suggest that if the dominant mass influx into the stream is constant and is unresponsive to surface hydrological conditions, dilution behavior is more likely to occur. The chemostatic behavior of geogenic elements (Na, Si, Ca, Mg) in 59 watersheds under different lithology, climatic, and hydrological conditions [*Godsey et al*., 2009] may indicate that groundwater mass influx of geogenic species is generally minor in headwater catchments. The more chemostatic CQ relationship observed in steep mountain catchments relative to those from shallow foreland floodplains may be due to the relatively dominant contribution of soil flow and mineral dissolution in steep watersheds [*Torres et al*., 2015]. Deep groundwater inputs into streams are likely to be higher in floodplains than upland watersheds [*Jencso et al*., 2010]. Characterization and quantification of groundwater influxes, however, often represent a major challenge [*Gellasch et al*., 2013; *Kuntz et al*., 2011; *Neal et al*., 1990; *Sellwood et al*., 2015].

5.3. Model Limitations and Challenges

RT-Flux-PIHM has the general disadvantages of parameter uncertainty and computation expenses as other distributed models [*Lu et al*., 2012; *Neuman et al*., 2012; *Ye et al*., 2004], in addition to the problem of scales and equifinality [*Beven*, 2006]. The interactions of deep groundwater with shallow soil water flow and streams need to be better constrained. Observed vertical variations in chemical and physical properties [*Andrews et al*., 2011; *Jin et al*., 2011a] are also simplified into a single homogeneous subsurface, which may have contributed to model-data discrepancy in reproducing chemical signatures. Including layered soil structure and properties

can be important for understanding processes of other chemical species. For example, dissolved organic carbon (DOC) are well known to be more abundant in top soils than in deep soils and therefore are important to be represented with layered structure [*Bishop et al*., 2004; *Grabs et al*., 2012]. However, inclusion of layered structure would require additional characterization and data that are often not available and are expensive to obtain.

In applying RT-Flux-PIHM to SSHCZO, we have avoided using a large number of parameters. Given the hydrological simulation from previous work [*Shi et al*., 2013], the groundwater influx was tuned to reproduce Cl data; and the clay dissolution kinetics (specific surface area) and cation exchange capacity were tuned to reproduce Mg data. The tuning of these parameters generated simulation results that are acceptable according to hydrology model standards, with simulation results in some locations more satisfactory than others (Figures 5 and 6). Future model refinement and rigorous model calibration may improve the model's match to data. Nonetheless, the CQ relationships, in particular the slopes of power law relation, $C=aQ^b$, are similar between model and data (Figures 8 and 10). The current implementation demonstrates synchronous hydrological and geochemical processes that may be affecting chemostasis at SSHCZO, which would have been difficult to evaluate without the new integrated model.

6. Conclusions

We use the newly developed, process-based watershed hydrogeochemical code RT-Flux-PIHM to explore the chemostatic behavior of Cl and Mg in SSHCZO. The connection between the hydrology module (PIHM), land surface module (Flux), and reactive transport module (RT) is the water content. The ability of simulating surface energy balance in Noah LSM improves the prediction of water fluxes such as evapotranspiration, total runoff (discharge), and peak discharge events, especially after extended dry periods. Accurate estimation of water fluxes is important in understanding and predicting geochemical processes at the watershed scale. For example, the model output shows Cl enrichment in soil in the summer because of the higher ET arising from the higher temperature and fully foliaged trees. Clay dissolution is also driven by the infiltration of new, fresh rainwater with its rates depending on water content and temperature.

Simulation results show that the dry watershed in the summer allows only low flow from a relatively small connected hillslope area to the stream, leading to Cl trapped in unconnected planar slopes. Large rainfall events wet and connect a large portion of the watershed, which flush out the trapped Cl and counteract the dilution effects brought about by the high V_w. These interdependent hydrological flow and Cl mobilization leads to Cl chemostatic behavior.

Similarly, simulation results indicate that Mg chemostasis is maintained by the synchrony between soil water content, lateral flow, and clay dissolution. The mass flux in stream discharge is dominated by subsurface lateral flow Q_L, which flushes Mg and is responsive to surface hydrological conditions. Simulation results show that surface area of dissolving clay grains in contact with flowing water (A_w) increases proportionally to the soil water content (V_w) and lateral flow Q_L. Chemostasis is therefore largely dictated by the roughly constant A_w/V_w ratio under varying hydrological conditions. In the summer, small A_w and consequently slower clay dissolution are compensated by small V_w and low Q_L. Large rainfall events increase V_w, Q_L, and A_w, therefore dissolving more clay and flushing out more Mg. This synchrony reflects the timely responsiveness of clay dissolution to hydrological changes. In contrast, under conditions where Mg influxes primarily come from deep groundwater that is unresponsive to surface hydrological conditions, dilution occurs. Compared to clay dissolution, cation exchange has a secondary effect on CQ relationship, although it does buffer Mg concentration by storing an order-of-magnitude higher magnesium on exchange sites than in soil water.

The model integrates complex hydrogeochemical processes to identify key controls of CQ relationships. Although the importance of individual processes, including clay dissolution and cation exchange in regulating stream chemistry, has been discussed in the literature [*Clow and Mast*, 2010; *Godsey et al*., 2009; *Herndon et al*., 2015], previous studies have used simplified, a priori conceptual models that highlight the importance of these individual processes. The advantage of process-based models lies in their capabilities of integrating multiple processes without a priori assumptions. Numerical experiments and sensitivity analysis can pinpoint the relative importance of competing processes, identify key drivers, while concurrently provide a holistic view of the system as a whole. As such it offers insights on process coupling and feedbacks that are important for the development of general principles and simplified explanatory framework. In addition, the

model allows the integration of watershed spatial characteristics (e.g., topography and land cover) and different types of data that have become largely available through concerted research efforts, to carry out virtual experiments for predicting watershed responses to changing climate, and to quantify elusive groundwater influxes [*Li et al*., 2017]. Although RT-Flux-PIHM suffers from similar limitation of distributed hydrological models in general [*Beven*, 2001, 2006], it holds the promise to resolve long-standing puzzles at the interface of hydrology and geochemistry.

Acknowledgments
This work was facilitated by NSF Critical Zone Observatory program grants to C.J.D. (EAR 07-25019) and S.L.B. (EAR 12-39285, EAR 13-31726). Data used in this research were collected in Penn State's Stone Valley Forest, which is supported and managed by the Penn State's Forestland Management Office in the College of Agricultural Sciences. These data have been digitized and are accessible through national CZO data portal (http://criticalzone.org/shale-hills/data/datasets/). All data are available at the Interdisciplinary Earth Data Alliance (IEDA) website [*Brantley and Sullivan*, 2014; *Brantley et al*., 2013b,c]. The source code for the model used in this study, RT-Flux-PIHM, and the input files necessary to reproduce the results are available from the authors upon request (lili@engr.psu.edu). We appreciate the Associate Editor Ming Ye and the Editor Jean Bahr for handling the manuscript and for providing insightful feedbacks on how to improve the manuscript. We acknowledge Jon Chorover, Lixin Jin, Gene-Hua Crystal Ng, and three anonymous reviewers for their constructive and meticulous reviews that have significantly improved the paper.

References

Anderson, S. P., W. E. Dietrich, R. Torres, D. R. Montgomery, and K. Loague (1997), Concentration-discharge relationships in runoff from a steep, unchanneled catchment, *Water Resour. Res.*, *33*(1), 211–225.

Andrews, D. M., H. Lin, Q. Zhu, L. Jin, and S. L. Brantley (2011), Hot spots and hot moments of dissolved organic carbon export and soil organic carbon storage in the shale hills catchment, *Vadose Zone J.*, *10*(3), 943–954.

Aylmore, L., I. Sills, and J. Quirk (1970), Surface area of homoionic illite and montmorillonite clay minerals as measured by the sorption of nitrogen and carbon dioxide, *Clays Clay Miner.*, *18*(2), 91–96.

Bao, C., L. Li, Y. Shi, and C. Duffy (2017), Understanding watershed hydrogeochemistry: 1. Development of RT-Flux-PIHM, *Water Resour. Res.*, *53*, doi:10.1002/2016WR018934.

Bastviken, D., F. Thomsen, T. Svensson, S. Karlsson, P. Sandén, G. Shaw, M. Matucha, and G. Öberg (2007), Chloride retention in forest soil by microbial uptake and by natural chlorination of organic matter, *Geochim. Cosmochim. Acta*, *71*(13), 3182–3192.

Basu, N. B., P. S. C. Rao, H. E. Winzeler, S. Kumar, P. Owens, and V. Merwade (2010a), Parsimonious modeling of hydrologic responses in engineered watersheds: Structural heterogeneity versus functional homogeneity, *Water Resour. Res.*, *46*, W04501, doi:10.1029/2009WR007803.

Basu, N. B., et al. (2010b), Nutrient loads exported from managed catchments reveal emergent biogeochemical stationarity, *Geophys. Res. Lett.*, *37*, L23404, doi:10.1029/2010GL045168.

Basu, N. B., S. E. Thompson, and P. S. C. Rao (2011), Hydrologic and biogeochemical functioning of intensively managed catchments: A synthesis of top-down analyses, *Water Resour. Res.*, *47*, W00J15, doi:10.1029/2011WR010800.

Beven, K. (2001), How far can we go in distributed hydrological modelling?, *Hydrol. Earth Syst. Sci.*, *5*(1), 1–12.

Beven, K. (2006), A manifesto for the equifinality thesis, *J. Hydrol.*, *320*(1–2), 18–36.

Bhatt, G., M. Kumar, and C. J. Duffy (2014), A tightly coupled GIS and distributed hydrologic modeling framework, *Environ. Modell. Software*, *62*, 70–84.

Bishop, K., J. Seibert, S. Köhler, and H. Laudon (2004), Resolving the Double Paradox of rapidly mobilized old water with highly variable responses in runoff chemistry, *Hydrol. Processes*, *18*(1), 185–189.

Boyer, E. W., G. M. Hornberger, K. E. Bencala, and D. M. McKnight (1997), Response characteristics of DOC flushing in an alpine catchment, *Hydrol. Processes*, *11*(12), 1635–1647.

Brandt, F., D. Bosbach, E. Krawczyk-Bärsch, T. Arnold, and G. Bernhard (2003), Chlorite dissolution in the acid pH-range: A combined microscopic and macroscopic approach, *Geochim. Cosmochim. Acta*, *67*(8), 1451–1461.

Brantley, S., T. White, A. White, D. Sparks, D. Richter, K. Pregitzer, L. Derry, J. Chorover, O. Chadwick, and R. April (2006), *Frontiers in Exploration of the Critical Zone: Report of a Workshop Sponsored by the National Science Foundation, October 24–26, 2005*, Univ. of Del., Newark.

Brantley, S. L., and P. L. Sullivan (2014), *Susquehanna Shale Hills Critical Zone Observatory Porewater Chemistry (2011)*, Integrated Earth Data Appl.

Brantley, S. L., M. E. Holleran, L. Jin, and E. Bazilevskaya (2013a), Probing deep weathering in the Shale Hills Critical Zone Observatory, Pennsylvania (USA): The hypothesis of nested chemical reaction fronts in the subsurface, *Earth Surf. Processes Landforms*, *38*(11), 1280–1298.

Brantley, S. L., L. Jin, D. Andrews, G. Holmes, M. Holleran, J. Z. Williams, E. Herndon, and P. L. Sullivan (2013b), *Susquehanna Shale Hills Critical Zone Observatory Porewater Chemistry (2008)*, Integrated Earth Data Appl.

Brantley, S. L., L. Jin, D. Andrews, G. Holmes, M. Bhatt, M. Holleran, N. Kaiser, J. Z. Williams, E. Herndon, and P. L. Sullivan (2013c), *Susquehanna Shale Hills Critical Zone Observatory Porewater Chemistry (2009)*, Integrated Earth Data Appl.

Brantley, S. L., et al. (2013d), *Susquehanna Shale Hills Critical Zone Observatory Stream Water Chemistry (2009)*, Integrated Earth Data Appl.

Buttle, J. M. (1994), Isotope hydrograph separations and rapid delivery of pre-event water from drainage basins, *Prog. Phys. Geogr.*, *18*(1), 16–41.

Chanat, J. G., K. C. Rice, and G. M. Hornberger (2002), Consistency of patterns in concentration-discharge plots, *Water Resour. Res.*, *38*(8), doi:10.1029/2001WR000971.

Clow, D. W., and M. A. Mast (2010), Mechanisms for chemostatic behavior in catchments: Implications for CO_2 consumption by mineral weathering, *Chem. Geol.*, *269*(1–2), 40–51.

Cussler, E. L. (2009), *Diffusion: Mass Transfer in Fluid Systems*, Cambridge Univ. Press, Cambridge, U. K.

Duffy, C., Y. Shi, K. Davis, R. Slingerland, L. Li, P. Sullivan, Y. Goddéris, and S. L. Brantley (2014), Designing a suite of models to explore critical zone function, *Procedia Earth Planet. Sci.*, *10*, 7–15.

Duffy, C. J., and J. Cusumano (1998), A low-dimensional model for concentration-discharge dynamics in groundwater stream systems, *Water Resour. Res.*, *34*(9), 2235–2247.

Evans, C., and T. D. Davies (1998), Causes of concentration/discharge hysteresis and its potential as a tool for analysis of episode hydrochemistry, *Water Resour. Res.*, *34*(1), 129–137.

Ferguson, R. (1986), River loads underestimated by rating curves, *Water Resour. Res.*, *22*(1), 74–76.

Gaillardet, J., B. Dupré, P. Louvat, and C. J. Allègre (1999), Global silicate weathering and CO_2 consumption rates deduced from the chemistry of large rivers, *Chem. Geol.*, *159*(1–4), 3–30.

Gautelier, M., E. H. Oelkers, and J. Schott (1999), An experimental study of dolomite dissolution rates as a function of pH from −0.5 to 5 and temperature from 25 to 80°C, *Chem. Geol.*, *157*(1), 13–26.

Gelhar, L. W., and J. L. Wilson (1974), Ground-water quality modeling, *Groundwater*, *12*(6), 399–408.

Gelhar, L. W., C. Welty, and K. R. Rehfeldt (1992), A critical review of data on field-scale dispersion in aquifers, *Water Resour. Res.*, *28*(7), 1955–1974.

Gellasch, C. A., K. R. Bradbury, D. J. Hart, and J. M. Bahr (2013), Characterization of fracture connectivity in a siliciclastic bedrock aquifer near a public supply well (Wisconsin, USA), *Hydrogeol. J.*, *21*(2), 383–399.

Godsey, S. E., J. W. Kirchner, and D. W. Clow (2009), Concentration–discharge relationships reflect chemostatic characteristics of US catchments, *Hydrol. Processes*, *23*(13), 1844–1864.
Grabs, T., K. Bishop, H. Laudon, S. W. Lyon, and J. Seibert (2012), Riparian zone hydrology and soil water total organic carbon (TOC): Implications for spatial variability and upscaling of lateral riparian TOC exports, *Biogeosciences*, *9*(10), 3901–3916.
Grimm, N. B., et al. (2003), Merging aquatic and terrestrial perspectives of nutrient biogeochemistry, *Oecologia*, *137*(4), 485–501.
Gupta, H. V., S. Sorooshian, and P. O. Yapo (1999), Status of automatic calibration for hydrologic models: Comparison with multilevel expert calibration, *J. Hydrol. Eng.*, *4*(2), 135–143.
Harmel, R. D., and P. K. Smith (2007), Consideration of measurement uncertainty in the evaluation of goodness-of-fit in hydrologic and water quality modeling, *J. Hydrol.*, *337*(3), 326–336.
Hasenmueller, E. A., L. Jin, G. E. Stinchcomb, H. Lin, S. L. Brantley, and J. P. Kaye (2015), Topographic controls on the depth distribution of soil CO_2 in a small temperate watershed, *Appl. Geochem.*, *63*, 58–69.
Helgeson, H. C., W. M. Murphy, and P. Aagaard (1984), Thermodynamic and kinetic constraints on reaction rates among minerals and aqueous solutions. II. Rate constants, effective surface area, and the hydrolysis of feldspar, *Geochim. Cosmochim. Acta*, *48*(12), 2405–2432.
Herndon, E. M., A. L. Dere, P. L. Sullivan, D. Norris, B. Reynolds, and S. L. Brantley (2015), Landscape heterogeneity drives contrasting concentration-discharge relationships in shale headwater catchments, *Hydrol. Earth Syst. Sci.*, *19*(8), 3333–3347.
Hoagland, B., T. A. Russo, X. Gu, L. Hill, J. Kaye, B. Forsythe, and S. L. Brantley (2017), Hyporheic zone influences on concentration-discharge relationships in a headwater sandstone stream, *Water Resour. Res.*, in press.
Hooper, R. P., N. Christophersen, and N. E. Peters (1990), Modelling streamwater chemistry as a mixture of soilwater end-members—An application to the Panola Mountain catchment, Georgia, USA, *J. Hydrol.*, *116*(1), 321–343.
Jencso, K. G., B. L. McGlynn, M. N. Gooseff, K. E. Bencala, and S. M. Wondzell (2010), Hillslope hydrologic connectivity controls riparian groundwater turnover: Implications of catchment structure for riparian buffering and stream water sources, *Water Resour. Res.*, *46*, W10524, doi:10.1029/2009WR008818.
Jin, L., R. Ravella, B. Ketchum, P. R. Bierman, P. Heaney, T. White, and S. L. Brantley (2010), Mineral weathering and elemental transport during hillslope evolution at the Susquehanna/Shale Hills Critical Zone Observatory, *Geochim. Cosmochim. Acta*, *74*(13), 3669–3691.
Jin, L., D. M. Andrews, G. H. Holmes, H. Lin, and S. L. Brantley (2011a), Opening the "black box": Water chemistry reveals hydrological controls on weathering in the Susquehanna Shale Hills Critical Zone Observatory, *Vadose Zone J.*, *10*(3), 928–942.
Jin, L., G. Rother, D. R. Cole, D. F. Mildner, C. J. Duffy, and S. L. Brantley (2011b), Characterization of deep weathering and nanoporosity development in shale—A neutron study, *Am. Mineral.*, *96*(4), 498–512.
Jin, L., N. Ogrinc, T. Yesavage, E. A. Hasenmueller, L. Ma, P. L. Sullivan, J. Kaye, C. Duffy, and S. L. Brantley (2014), The CO_2 consumption potential during gray shale weathering: Insights from the evolution of carbon isotopes in the Susquehanna Shale Hills Critical Zone Observatory, *Geochim. Cosmochim. Acta*, *142*, 260–280.
Johnson, N. M., G. E. Likens, F. H. Bormann, D. W. Fisher, and R. S. Pierce (1969), A working model for the variation in stream water chemistry at the Hubbard Brook Experimental Forest, New Hampshire, *Water Resour. Res.*, *5*(6), 1353–1363.
Kirchner, J. W. (2003), A double paradox in catchment hydrology and geochemistry, *Hydrol. Processes*, *17*(4), 871–874.
Kirchner, J. W., X. Feng, and C. Neal (2000), Fractal stream chemistry and its implications for contaminant transport in catchments, *Nature*, *403*(6769), 524–527.
Kirchner, J. W., X. Feng, and C. Neal (2001), Catchment-scale advection and dispersion as a mechanism for fractal scaling in stream tracer concentrations, *J. Hydrol.*, *254*(1), 82–101.
Köhler, S. J., F. Dufaud, and E. H. Oelkers (2003), An experimental study of illite dissolution kinetics as a function of pH from 1.4 to 12.4 and temperature from 5 to 50°C, *Geochim. Cosmochim. Acta*, *67*(19), 3583–3594.
Köhler, S. J., D. Bosbach, and E. H. Oelkers (2005), Do clay mineral dissolution rates reach steady state?, *Geochim. Cosmochim. Acta*, *69*(8), 1997–2006.
Kumar, M., C. J. Duffy, and K. M. Salvage (2009), A second-order accurate, Finite Volume-Based, Integrated Hydrologic Modeling (FIHM) framework for simulation of surface and subsurface flow, *Vadose Zone J.*, *8*(4), 873–890.
Kuntz, B. W., S. Rubin, B. Berkowitz, and K. Singha (2011), Quantifying solute transport at the Shale Hills Critical Zone Observatory, *Vadose Zone J.*, *10*(3), 843–857.
Lamb, D., and V. Bowersox (2000), The National Atmospheric Deposition Program: An overview, *Atmos. Environ.*, *34*(11), 1661–1663.
Lasaga, A. C. (1984), Chemical kinetics of water-rock interactions, *J. Geophys. Res.*, *89*(B6), 4009–4025.
Legates, D. R., and G. J. McCabe (1999), Evaluating the use of "goodness-of-fit" measures in hydrologic and hydroclimatic model validation, *Water Resour. Res.*, *35*(1), 233–241.
Li, L., F. Salehikhoo, S. L. Brantley, and P. Heidari (2014), Spatial zonation limits magnesite dissolution in porous media, *Geochim. Cosmochim. Acta*, *126*, 555–573.
Li, L., et al. (2017), Expanding the role of reactive transport models in critical zone processes, *Earth Sci. Rev.*, *165*, 280–301.
Lin, H. (2006), Temporal stability of soil moisture spatial pattern and subsurface preferential flow pathways in the Shale Hills Catchment, *Vadose Zone J.*, *5*(1), 317–340.
Lu, D., M. Ye, S. P. Neuman, and L. Xue (2012), Multimodel Bayesian analysis of data-worth applied to unsaturated fractured tuffs, *Adv. Water Resour.*, *35*, 69–82.
Ma, L., F. Chabaux, E. Pelt, E. Blaes, L. Jin, and S. Brantley (2010), Regolith production rates calculated with uranium-series isotopes at Susquehanna/Shale Hills Critical Zone Observatory, *Earth Planet. Sci. Lett.*, *297*(1–2), 211–225.
Maher, K. (2011), The role of fluid residence time and topographic scales in determining chemical fluxes from landscapes, *Earth Planet. Sci. Lett.*, *312*(1–2), 48–58.
Mayer, K. U., E. O. Frind, and D. W. Blowes (2002), Multicomponent reactive transport modeling in variably saturated porous media using a generalized formulation for kinetically controlled reactions, *Water Resour. Res.*, *38*(9), 1174, doi:10.1029/2001WR000862.
Moore, D. M., and R. C. Reynolds (1989), *X-ray Diffraction and the Identification and Analysis of Clay Minerals*, Oxford Univ. Press, Oxford, U. K.
Moore, J., P. C. Lichtner, A. F. White, and S. L. Brantley (2012), Using a reactive transport model to elucidate differences between laboratory and field dissolution rates in regolith, *Geochim. Cosmochim. Acta*, *93*, 235–261.
Moriasi, D. N., J. G. Arnold, M. W. Van Liew, R. L. Bingner, R. D. Harmel, and T. L. Veith (2007), Model evaluation guidelines for systematic quantification of accuracy in watershed simulations, *Trans. ASABE*, *50*(3), 885–900.
Nash, J. E., and J. V. Sutcliffe (1970), River flow forecasting through conceptual models part I—A discussion of principles, *J. Hydrol.*, *10*(3), 282–290.
Navarre-Sitchler, A., and S. Brantley (2007), Basalt weathering across scales, *Earth Planet. Sci. Lett.*, *261*(1), 321–334.

Neal, C., A. Robson, and C. J. Smith (1990), Acid neutralization capacity variations for the Hafren Forest stream, mid-Wales: Inferences for hydrological processes, *J. Hydrol.*, *121*(1), 85–101.
Neal, C., T. Hill, S. Alexander, B. Reynolds, S. Hill, A. J. Dixon, M. Harrow, M. Neal, and C. J. Smith (1997a), Stream water quality in acid sensitive UK upland areas; an example of potential water quality remediation based on groundwater manipulation, *Hydrol. Earth Syst. Sci. Discuss.*, *1*(1), 185–196.
Neal, C., A. Robson, P. Shand, W. Edmunds, A. Dixon, D. Buckley, S. Hill, M. Harrow, M. Neal, and J. Wilkinson (1997b), The occurrence of groundwater in the Lower Palaeozoic rocks of upland Central Wales, *Hydrol. Earth Syst. Sci. Discuss.*, *1*(1), 3–18.
Neuman, S. P., L. Xue, M. Ye, and D. Lu (2012), Bayesian analysis of data-worth considering model and parameter uncertainties, *Adv. Water Resour.*, *36*, 75–85.
Peters, N. E., E. B. Ratcliffe, and M. Tranter (1998), *Tracing solute mobility at the Panola Mountain Research Watershed*, Georgia, USA: Variations in Na^+, Cl^-, and H_4SiO_4 concentrations, *IAHS Publ.*, 483–490.
Pokrovsky, O. S., S. V. Golubev, and J. Schott (2005), Dissolution kinetics of calcite, dolomite and magnesite at 25°C and 0 to 50 atm pCO_2, *Chem. Geol.*, *217*(3), 239–255.
Qu, Y., and C. J. Duffy (2007), A semidiscrete finite volume formulation for multiprocess watershed simulation, *Water Resour. Res.*, *43*, W08419, doi:10.1029/2006WR005752.
Raymond, P. A., and J. J. Cole (2003), Increase in the export of alkalinity from North America's largest river, *Science*, *301*(5629), 88–91.
Rice, K. C., and G. M. Hornberger (1998), Comparison of hydrochemical tracers to estimate source contributions to peak flow in a small, forested, headwater catchment, *Water Resour. Res.*, *34*(7), 1755–1766.
Salehikhoo, F., and L. Li (2015), The role of magnesite spatial distribution patterns in determining dissolution rates: When do they matter?, *Geochim. Cosmochim. Acta*, *155*, 107–121.
Sebestyen, S. D., E. W. Boyer, J. B. Shanley, C. Kendall, D. H. Doctor, G. R. Aiken, and Ohte, N. (2008), Sources, transformations, and hydrological processes that control stream nitrate and dissolved organic matter concentrations during snowmelt in an upland forest, *Water Resour. Res.*, *44*, W12410, doi:10.1029/2008WR006983.
Sebestyen, S. D., J. B. Shanley, E. W. Boyer, C. Kendall, and D. H. Doctor (2014), Coupled hydrological and biogeochemical processes controlling variability of nitrogen species in streamflow during autumn in an upland forest, *Water Resour. Res.*, *50*, 1569–1591, doi:10.1002/2013WR013670.
Sellwood, S. M., D. J. Hart, and J. M. Bahr (2015), An in-well heat-tracer-test method for evaluating borehole flow conditions, *Hydrogeol. J.*, *23*(8), 1817–1830.
Semenov, M. Y., and E. A. Zimnik (2015), A three-component hydrograph separation based on relationship between organic and inorganic component concentrations: A case study in Eastern Siberia, Russia, *Environ. Earth Sci.*, *73*(2), 611–620.
Sherman, L. A., and P. Barak (2000), Solubility and dissolution kinetics of dolomite in Ca–Mg–HCO/CO solutions at 25°C and 0.1 MPa carbon dioxide, *Soil Sci. Soc. Am. J.*, *64*(6), 1959–1968.
Shi, Y., K. J. Davis, C. J. Duffy, and X. Yu (2013), Development of a coupled land surface hydrologic model and evaluation at a critical zone observatory, *J. Hydrometeorol.*, *14*(5), 1401–1420.
Stallard, R. F., and S. F. Murphy (2014), A unified assessment of hydrologic and biogeochemical responses in research watersheds in eastern Puerto Rico using runoff–concentration relations, *Aquat. Geochem.*, *20*(2–3), 115–139.
Stenback, G. A., W. G. Crumpton, K. E. Schilling, and M. J. Helmers (2011), Rating curve estimation of nutrient loads in Iowa rivers, *J. Hydrol.*, *396*(1–2), 158–169.
Svensson, T., P. Sandén, D. Bastviken, and G. Öberg (2007), Chlorine transport in a small catchment in southeast Sweden during two years, *Biogeochemistry*, *82*(2), 181–199.
Svensson, T., G. M. Lovett, and G. E. Likens (2012), Is chloride a conservative ion in forest ecosystems?, *Biogeochemistry*, *107*(1–3), 125–134.
Thomas, E. M., H. Lin, C. J. Duffy, P. L. Sullivan, G. H. Holmes, S. L. Brantley, and L. Jin (2013), Spatiotemporal patterns of water stable isotope compositions at the Shale Hills Critical Zone Observatory: Linkages to subsurface hydrologic processes, *Vadose Zone J.*, *12*(4).
Thompson, S. E., N. B. Basu, J. Lascurain Jr., A. Aubeneau, and P. S. C. Rao (2011), Relative dominance of hydrologic versus biogeochemical factors on solute export across impact gradients, *Water Resour. Res.*, *47*, W00J05, doi:10.1029/2010WR009605.
Torres, M. A., A. J. West, and K. E. Clark (2015), Geomorphic regime modulates hydrologic control of chemical weathering in the Andes–Amazon, *Geochim. Cosmochim. Acta*, *166*, 105–128.
Weaver, C. E. (1989), *Clays, Muds, and Shales*, Elsevier, New York.
Wen, H., L. Li, D. Crandall, and J. A. Hakala (2016), Where lower calcite abundance creates more alteration: Enhanced rock matrix diffusivity induced by preferential carbonate dissolution, *Energy Fuels*, *30*(5), 4197–4208.
White, A. F., and A. E. Blum (1995), Effects of climate on chemical weathering in watersheds, *Geochim. Cosmochim. Acta*, *59*(9), 1729–1747.
White, A. F., and S. L. Brantley (2003), The effect of time on the weathering of silicate minerals: Why do weathering rates differ in the laboratory and field?, *Chem. Geol.*, *202*(3–4), 479–506.
Wolery, T. J. (1992), EQ3/6: A Software Package for Geochemical Modeling of Aqueous Systems: Package Overview and Installation Guide (*Version 7.0*), Lawrence Livermore Natl. Lab., Livermore, Calif.
Ye, M., S. P. Neuman, and P. D. Meyer (2004), Maximum likelihood Bayesian averaging of spatial variability models in unsaturated fractured tuff, *Water Resour. Res.*, *40*, W05113, doi:10.1029/2003WR002557.